INSTITUTE OF PHYSICS PUBLISHING WAVES IN RANDOM MEDIA

Waves Random Media **14** (2004) 253–276 PII: S0959-7174(04)69411-0

Multiple scattering in the high-frequency limit with second-order shadowing function from 2D anisotropic rough dielectric surfaces: II. Comparison with numerical results

C Bourlier[1] **and G Berginc**[2]

[1] IREENA, Radar Team, Ecole polytechnique de l'université de Nantes—Bat. IRESTE, Rue Christian Pauc, La Chantrerie, BP 50609, 44306 Nantes Cedex 3, France
[2] DS/DFO, THALES Optronique, Rue Guynemer, BP 55, 78283 Guyancourt Cedex, France

E-mail: christophe.bourlier@polytech.univ-nantes.fr

Received 23 September 2003, in final form 19 February 2004
Published 31 March 2004
Online at stacks.iop.org/WRM/14/253 (DOI: 10.1088/0959-7174/14/3/004)

Abstract

This second part presents illustrative examples of the model developed in the companion paper, which is based on the first- and second-order optics approximation. The surface is assumed to be Gaussian and the correlation height is chosen as anisotropic Gaussian. The incoherent scattering coefficient is computed for a height rms range from 0.5λ to 1λ (where λ is the electromagnetic wavelength), for a slope rms range from 0.5 to 1 and for an incidence angle range from 0 to 70°. In addition, simulations are presented for an anisotropic Gaussian surface and when the receiver is not located in the plane of incidence. For a metallic and dielectric isotropic Gaussian surfaces, the cross- and co-polarizations are also compared with a numerical approach obtained from the forward–backward method with a novel spectral acceleration algorithm developed by Torrungrueng and Johnson (2001, *JOSA* A **18**).

(Some figures in this article are in colour only in the electronic version)

1. Introduction

In this second part, the incoherent scattering coefficient obtained under the one- and second-order geometric optics approximation is simulated for an anisotropic Gaussian surface and compared with numerical results [1], for which the height correlation function is assumed to be Gaussian. Dielectric and metallic surfaces, rms slope ranging from 0.5 to 1 and rms height ranging from 0.5λ to 1λ, are considered in this study, where λ is the electromagnetic wavelength. In addition, the incoherent scattering coefficient is computed for incident angles ranging from normal incidence up to 70°, for which nonlocal interactions and increased

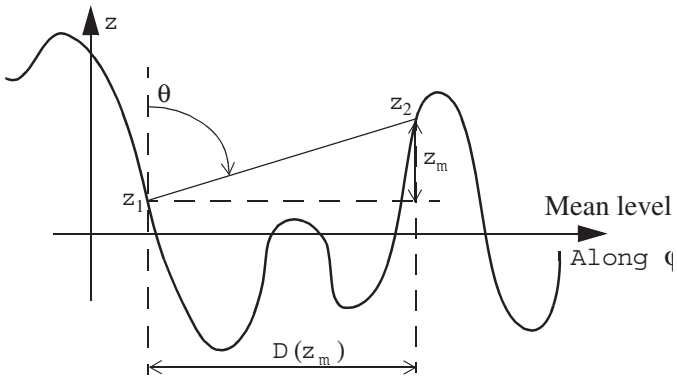

Figure 1. Geometric representation of the mean duration of a fade $D(z_m)$ for a given height level z_m.

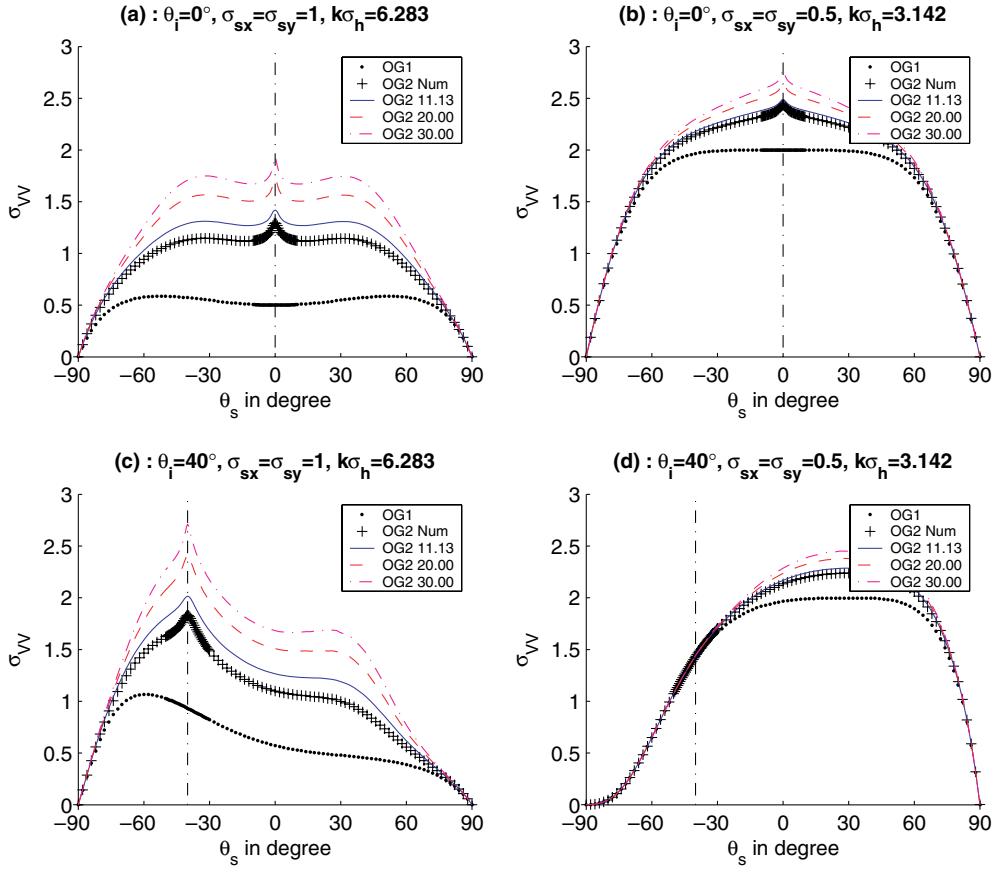

Figure 2. Incoherent scattering coefficient σ_{VV} in VV polarization versus the scattering angle θ_i for an isotropic ($\sigma_{sx} = \sigma_{sy}$) metallic surface. At the top, the incidence angle $\theta_i = 0^\circ$, whereas at the bottom $\theta_i = 40^\circ$. On the left, $\sigma_{sx} = 1$ and $k\sigma_h = 2\pi \Rightarrow \sigma_h/\lambda = 1$ (wave number k multiplied by rms height σ_h), whereas on the right, $\sigma_{sx} = 0.5$ and $k\sigma_h = \pi \Rightarrow \sigma_h/\lambda = 0.5$. The receiver and the transmitter are located in the same plane and $\varphi_s = \varphi_i = 0^\circ$.

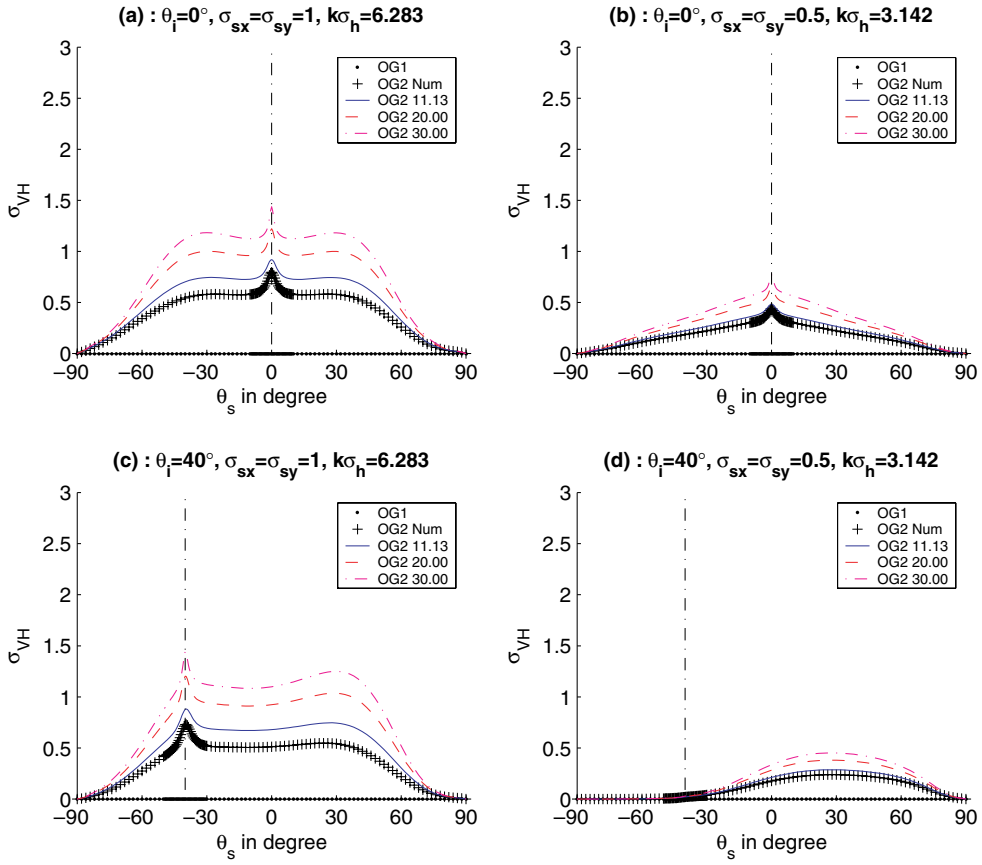

Figure 3. Same variation as figure 2 in VH polarization.

shadowing effects are involved. Simulations are also presented when the surface is anisotropic unlike papers [1–3].

Whereas the scattering models [4–6] from one-dimensional (1D) may be adequate for co-polarized scattering, a 2D surface model is required for predicting cross-polarized scattering. Since backscattering enhancement is related to multiple-scattering effects, cross-polarized fields should illustrate the backscattering enhancement effect more clearly than co-polarized fields.

This paper is organized as follows. From [7], in section 2, expressions of the first- and second-order incoherent scattering coefficients are presented by assuming an anisotropic Gaussian process. In section 3, the present model is compared with numerical results and the last section gives concluding remarks.

2. Incoherent scattering coefficient for a Gaussian process

In this section, for the special case of a Gaussian process, the first- and second-order Kirchhoff approximations presented in the companion paper are summarized. The bistatic incoherent cross section of waves scattered from two-dimensional rough anisotropic surfaces is then expressed as

$$\sigma_t = \sigma_1 + \sigma_{12} + \sigma_2. \tag{1}$$

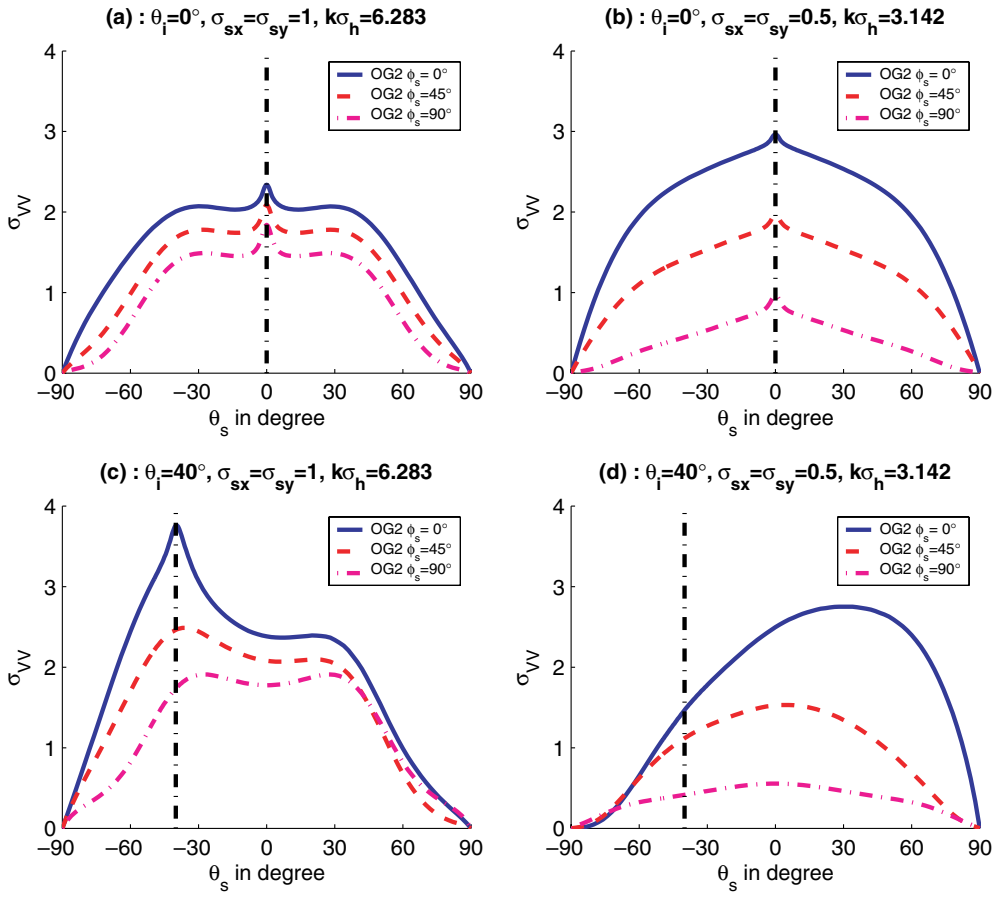

Figure 4. Same variation as figure 2 but $\varphi_s = \{0, 45, 90\}^\circ$ as indicated in the legend and $l_m = 11.13 L_{cx}$.

2.1. Incoherent scattering coefficient in the high-frequency limit

σ_1 is referred to as the first-order Kirchhoff term giving the contribution of the single scattering under the geometric optics assumption ((26) of [7])

$$\sigma_1 = \frac{\pi |k \bar{F}_1(\hat{\boldsymbol{K}}_i, \hat{\boldsymbol{K}}_s)|^2}{(q_s - q_i)^2} p_s\left(\boldsymbol{s}_1^0\right) S_1\left(\hat{\boldsymbol{K}}_i, \hat{\boldsymbol{K}}_s \mid \boldsymbol{s}_1^0\right) \cdot \tag{2}$$

$\boldsymbol{s}_1^0$ ((26*a*) of [7]) are the surface slopes defined as the specular direction and $k_0 = 2\pi/\lambda$ stands for the wave number with λ being the electromagnetic wavelength. $\bar{F}_1(\hat{\boldsymbol{K}}_i, \hat{\boldsymbol{K}}_s)$ is a square matrix of length 2 related to the polarization terms expressed in appendix A of [7]. $\{\hat{\boldsymbol{K}}_i, \hat{\boldsymbol{K}}_s\}$ are the unitary incident and scattered wave vectors defined as $\hat{\boldsymbol{K}}_i = \hat{\boldsymbol{k}}_i + \hat{q}_i \hat{\boldsymbol{z}}$ and $\hat{\boldsymbol{K}}_s = \hat{\boldsymbol{k}}_s + \hat{q}_s \hat{\boldsymbol{z}}$ where $q_i = -k \cos\theta_i$ and $q_s = k \cos\theta_s \cdot p_s\left(\boldsymbol{s}_1^0\right)$ is the surface slope probability density function expressed for an anisotropic Gaussian process as

$$p_s(\boldsymbol{s}_1) = \frac{1}{2\pi \sigma_{sx} \sigma_{sy}} \exp\left(-\frac{s_{1x}^2}{2\sigma_{sx}^2} - \frac{s_{1y}^2}{2\sigma_{sy}^2}\right), \tag{3}$$

where $\{\sigma_{sx}, \sigma_{sy}\}$ are the rms slope with respect to the directions $\{\hat{\boldsymbol{x}}, \hat{\boldsymbol{y}}\}$. Since the height correlation function is assumed to be even, the cross-correlation between the slopes $\{s_{1x}, s_{1y}\}$

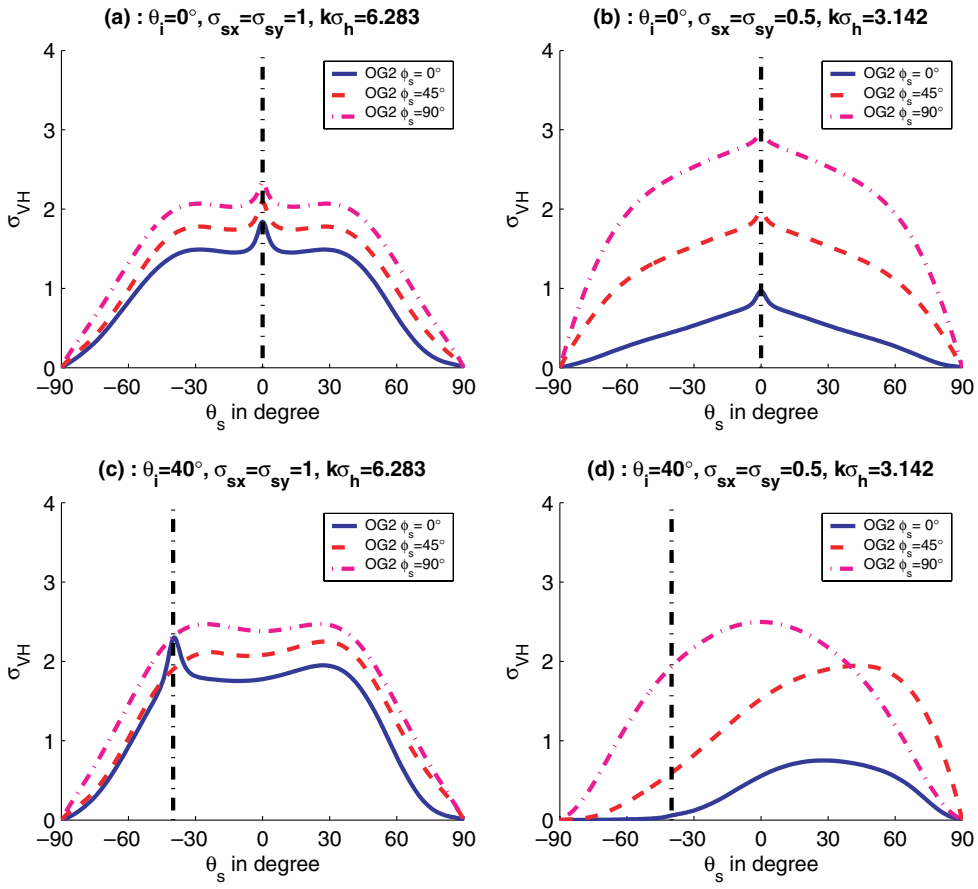

Figure 5. Same variation as figure 4 but in VH polarization.

is nil. $S_1\big(\hat{\boldsymbol{K}}_i, \hat{\boldsymbol{K}}_s \,\big|\, \boldsymbol{s}_1^0\big)$ denotes the average bistatic shadowing function over the surface elevations and with the knowledge of the slope $\boldsymbol{s}_1^0$. It is given by (48), (49) and (51) of [7] for $\varphi_s = \varphi_i, \varphi_s = \varphi_i + \pi$ and $\{\varphi_s \neq \varphi_i, \varphi_s \neq \varphi_i + \pi\}$ (transmitter of azimuthal angle φ_i and receiver of azimuth angle φ_s in different planes), respectively, in which $\Lambda(\hat{\boldsymbol{K}})$ has to be derived. In [8], a method is addressed for the derivation of $\Lambda(\hat{\boldsymbol{K}})$. For a Gaussian process, $\Lambda(\hat{\boldsymbol{K}})$ then takes the form

$$\Lambda(\hat{\boldsymbol{K}}) \equiv \Lambda(\nu) = [\exp(-\nu^2) - \nu\sqrt{\pi}\operatorname{erfc}(\nu)]/(2\nu\sqrt{\pi}), \qquad \text{and}$$
$$\nu = \frac{|\cot\theta|}{\sqrt{2\big[\sigma_{sx}^2(\cos\varphi)^2 + \sigma_{sy}^2(\sin\varphi)^2\big]}}. \tag{4}$$

where erfc is the complementary error function.

In the high-frequency limit, the contribution of the cross-Kirchhoff term σ_{12}, related to the correlation between the first- and second-order scattered field, is equal to zero due to the shadow.

The second-order scattering coefficient is expressed as the sum of two terms $\sigma_2 = \sigma_{2c} + \sigma_{2a}$.

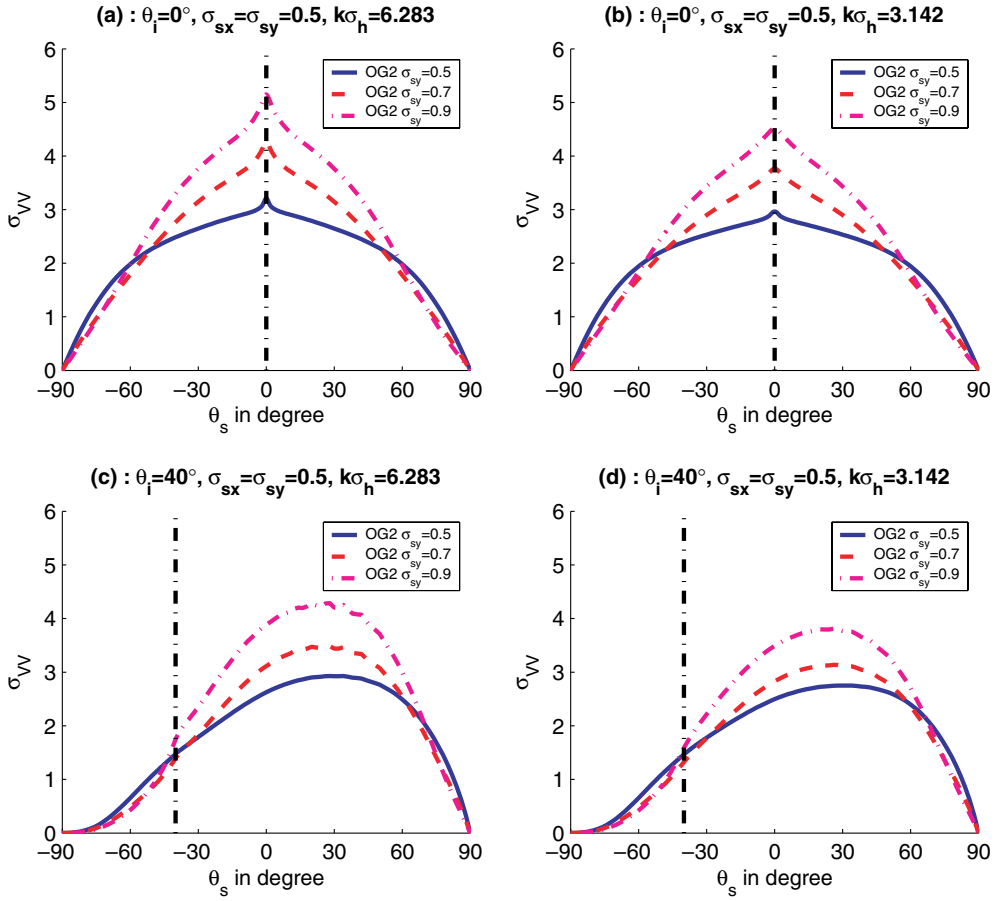

Figure 6. Same variation as figure 2 but $\sigma_{sy} \neq \sigma_{sx}$ ($\sigma_{sx} = 0.5$, $\sigma_{sy} = \{0.5, 0.7, 0.9\}$ as indicated in the legend) and $l_m = 11.13 L_{cx}$.

In the high-frequency limit, the incoherent scattering coefficient related to the coincidental waves (subscript c) is given by ((41) of [7])

$$\sigma_{2c} = \frac{\pi k^4}{16} \int_0^{\pi/2} \mathrm{d}\theta \int_0^{\pi/2} \mathrm{d}\theta' \int_0^{2\pi} \mathrm{d}\varphi \int_0^{2\pi} \mathrm{d}\varphi' \frac{|\bar{F}_{1m}(\hat{\boldsymbol{K}}_i, \hat{\boldsymbol{K}}'_m, \hat{\boldsymbol{K}}_s)|^2 \chi_t(\boldsymbol{k} - \boldsymbol{k}') \sin\theta \sin\theta'}{(\pm q' - q_i)^2 (\pm q' - q_s)^2},$$
$$p_s\left(\boldsymbol{s}_1^{0c}\right) p_s\left(\boldsymbol{s}_2^{0c}\right) \left\langle S_c\left(\hat{\boldsymbol{K}}_i, \hat{\boldsymbol{K}}_m, \hat{\boldsymbol{K}}_s \,\middle|\, \boldsymbol{s}_1^{0c}, \boldsymbol{s}_2^{0c}, z_{21}\right) \exp[m\mathrm{j}(q - q')z_{21}] \right\rangle \tag{5}$$

where the slopes $\left\{\boldsymbol{s}_{1,2}^{0c}\right\}$ are given by

$$\boldsymbol{s}_1^{0c} = -(\boldsymbol{k}' - \boldsymbol{k}_i)/(mq' - q_i), \qquad \boldsymbol{s}_2^{0c} = -(\boldsymbol{k}' - \boldsymbol{k}_s)/(mq' - q_s) \quad \text{and} \quad m = \pm. \tag{5a}$$

When $m = +$, σ_{2c} gives the contribution of the wave positive paths where $z_{21} = z_2 - z_1 \geqslant 0$, whereas for $m = -$, σ_{2c} gives the contribution of the wave negative paths where $z_{21} = z_2 - z_1 < 0$. $\{z_i\}$ is the elevation at the point (i) on the surface. $\bar{F}_{1m}(\hat{\boldsymbol{K}}_i, \hat{\boldsymbol{K}}_m, \hat{\boldsymbol{K}}_s) = \bar{F}_1(\hat{\boldsymbol{K}}_i, \hat{\boldsymbol{K}}_m) \bar{F}_1(\hat{\boldsymbol{K}}_{-m}, \hat{\boldsymbol{K}}_s)$ is a square matrix defined from a matrix product, where $\bar{F}_1$

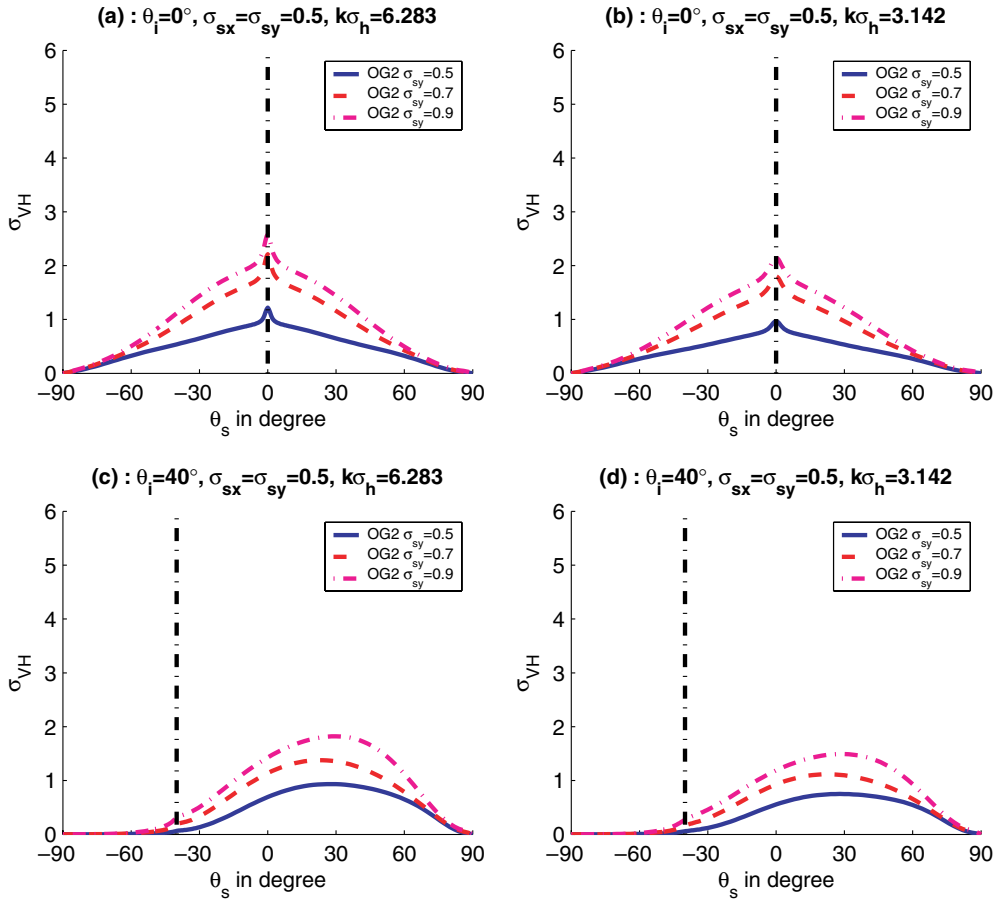

Figure 7. Same variation as figure 6 but in VH polarization.

related to the polarization terms is expressed in appendix A of [7]. It must be noted that $\bar{F}_{1+}(\hat{\boldsymbol{K}}_i, \hat{\boldsymbol{K}}_+, \hat{\boldsymbol{K}}_s) = F_{1-}(\hat{\boldsymbol{K}}_s, \hat{\boldsymbol{K}}_-, \hat{\boldsymbol{K}}_i)$ which ensures the reciprocity.

The incoherent scattering coefficient related to the anticoincidental waves (subscript a) is given by ((43) of [7])

$$\sigma_{2a} = \frac{\pi k^4}{8}\,\mathrm{Re}\Bigg\{\int_0^{\pi/2}\mathrm{d}\theta\int_0^{\pi/2}\mathrm{d}\theta'\int_0^{2\pi}\mathrm{d}\varphi\int_0^{2\pi}\mathrm{d}\varphi' \times \frac{|\bar{F}_{1-}(\hat{\boldsymbol{K}}_i, \hat{\boldsymbol{K}}'_-, \hat{\boldsymbol{K}}_s)|^2 \sin\theta\sin\theta' p_s\big(\boldsymbol{s}_1^{0a}\big) p_s\big(\boldsymbol{s}_2^{0a}\big)}{(q'+q_s)^2(q'+q_i)^2} \times \chi_t(\boldsymbol{k}+\boldsymbol{k}'-\boldsymbol{k}_i-\boldsymbol{k}_s)\big\langle S_a\big(\hat{\boldsymbol{K}}_i, \hat{\boldsymbol{K}}'_-, \hat{\boldsymbol{K}}_s \,\big|\, \boldsymbol{s}_1^{0a}, \boldsymbol{s}_2^{0a}, z_{21}\big) \times \exp[\,\mathrm{j}(q-q'-q_i-q_s)z_{21}]\big\rangle\Bigg\}, \tag{6}$$

where

$$\boldsymbol{s}_1^{0a} = -(\boldsymbol{k}_s - \boldsymbol{k}')/(q_s+q'), \qquad \boldsymbol{s}_2^{0a} = -(\boldsymbol{k}_i - \boldsymbol{k}')/(q_i+q'). \tag{6a}$$

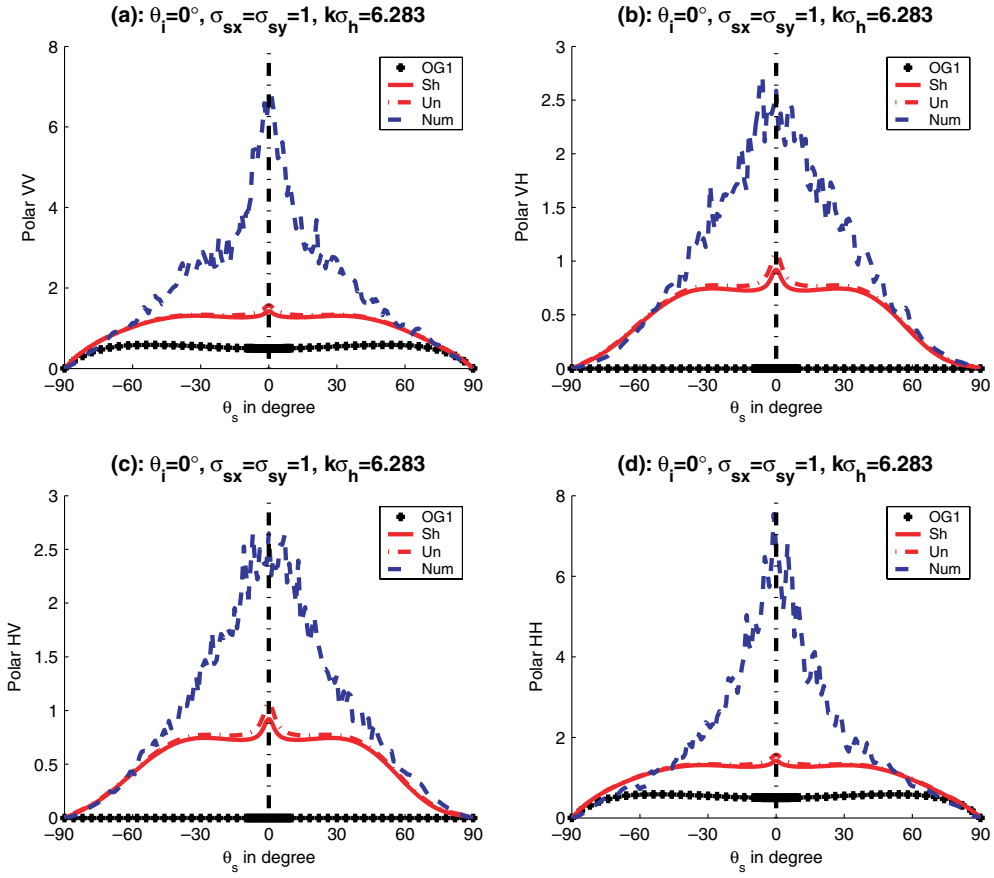

Figure 8. Comparison of the geometric optics approximation denoted as 'OG1' (first order), 'Sh' (first and second orders with shadow) and 'Un' (first and second orders without shadow) with numerical results [1] referred to as 'Num' for {VV (a), VH (b), HV (c), HH (d)} polarizations. The surface is assumed to be metallic and isotropic. $l_m = 11.13L_{cx}$, $\sigma_{sy} = \sigma_{sx} = 1$, $k\sigma_h = 2\pi \Rightarrow \sigma_h/\lambda = 1$ and incidence angle $\theta_i = 0°$.

2.2. *Tapering function*

In (5) and (6), the function $\chi_t(\boldsymbol{u})$ is defined as

$$\chi_t(\boldsymbol{u}) = \left(\frac{k}{\pi}\right)^2 \int S_t(\boldsymbol{u}) \exp(\mathrm{j}\boldsymbol{u}\cdot\mathbf{r}_{21})\,\mathrm{d}\mathbf{r}_{21}. \tag{7}$$

$S_t(\boldsymbol{u})$ is a tapering function which quantifies the fact that the scattered waves at the point (1) propagate only in a certain distance before being intercepted by the surface at the point (2) (see figure 4 of [7]). Ishimaru *et al* [5] set $S_t(\boldsymbol{u}) = \exp\left(-\boldsymbol{u}^2/l_m^2\right)$ (which is similar to add an apodization function) and Bahar *et al* [6] used $S_t(\boldsymbol{u}) = \Pi_{[-l_m;l_m]} = 1$ if $\|\boldsymbol{u}\| \in [-l_m; l_m]$ else 0.

For a one-dimensional surface, we compared the incoherent scattering coefficient according to $S_t(\boldsymbol{u})$. The simulations showed that the results are similar for both these functions S_t. Thus, for the simulations we chose the one used by Ishimaru *et al* because in (5) and (6) the integration over φ can be derived analytically (see appendix A). This leads to

$$\chi_t(\boldsymbol{u}) = (kl_m)^2 \exp\left(-l_m^2\boldsymbol{u}^2/2\right)/\pi. \tag{8}$$

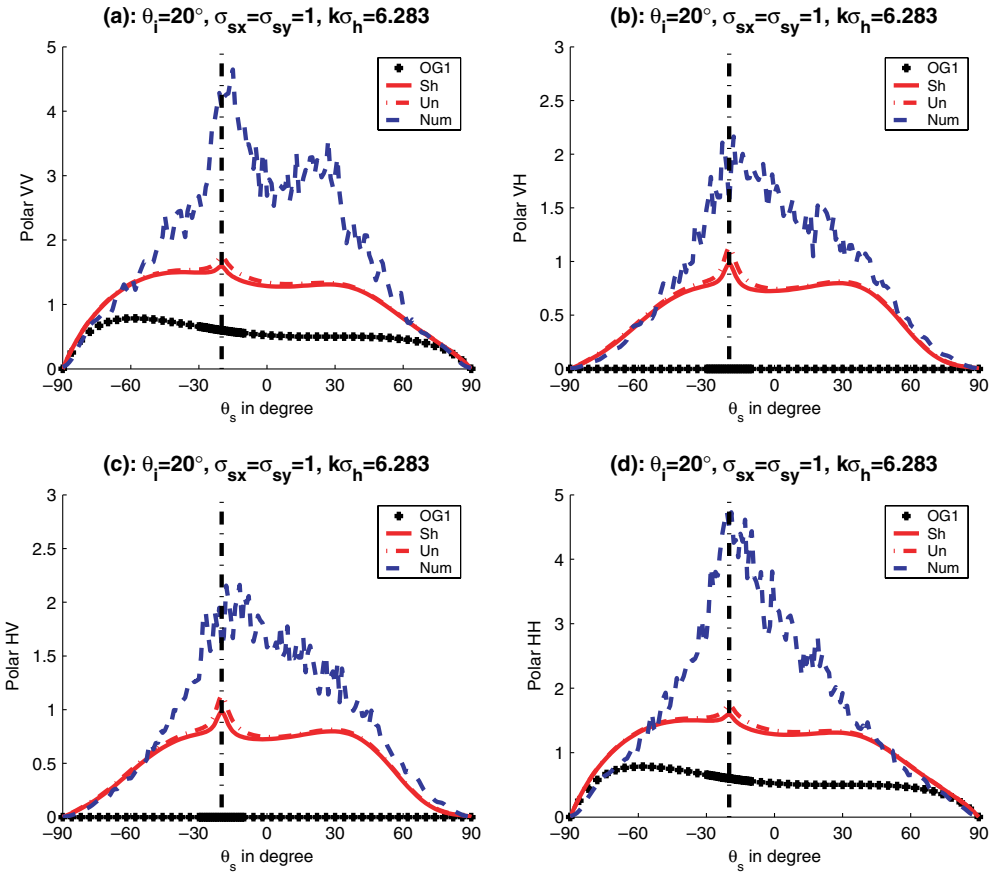

Figure 9. Same variation as figure 8 but $\theta_i = 20^\circ$.

In the above equation, the calculation of χ_t requires the knowledge of the mean path length l_m. To calculate l_m, Ishimaru *et al* [4, 5] identified this length as the mean duration of a fade and they showed for a Gaussian process with a Gaussian height correlation that

$$D(z_m)/L_c = \frac{\pi}{\sqrt{2}} \exp\left(\frac{z_m^2}{2\sigma_h^2}\right)\left[1 + \operatorname{erf}\left(\frac{z_m}{\sqrt{2}\sigma_h}\right)\right] \qquad \text{and} \qquad l_m = D(z_m)|_{z_m \sim \sigma_h}. \tag{9}$$

In addition, $z_m = \sigma_h\sqrt{2}$ which satisfies power conservation for a Dirichlet one-dimensional Gaussian surface and is consistent with sinusoidal surfaces. This leads to $l_m = 11.13 L_{cx,cy}$ where $\{L_{cx,cy}\}$ are the correlation lengths with respect to the directions $\{\hat{\boldsymbol{x}}, \hat{\boldsymbol{y}}\}$. As depicted in figure 1, z_m depends on the angles $\{\theta, \varphi\}$ and the slope rms $\{\sigma_{sx}, \sigma_{sy}\}$ are not taken into account in (9). From the second-order shadowing function, appendix C proposes a method for the derivation of $z_m = z_m(\nu) \equiv z_m(\theta, \varphi, \sigma_{sx}, \sigma_{sy})$ where ν is given from (4).

2.3. Second-order shadowing function

To calculate in (5), the ensemble average $\langle \cdots \rangle$ over $z_{21} = z_2 - z_1$, the shadowing effect is assumed to be statistically independent of $\exp[mj(q - q')z_{21}]$ leading to

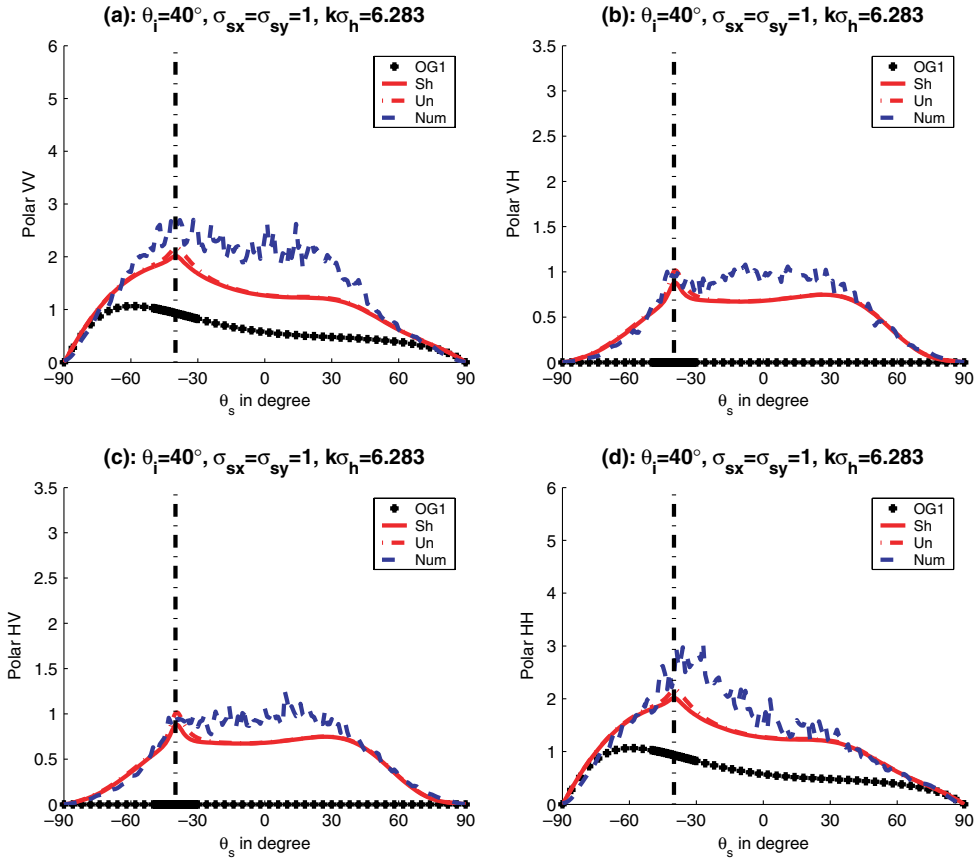

Figure 10. Same variation as figure 8 but $\theta_i = 40^\circ$.

$$\begin{aligned}&\left\langle S_c\left(\hat{\boldsymbol{K}}_i, \hat{\boldsymbol{K}}_m, \hat{\boldsymbol{K}}_s \,\middle|\, s_1^{0c}, s_2^{0c}, z_{21}\right) \exp[mj(q-q')z_{21}]\right\rangle \\ &\qquad = \left\langle S_c\left(\hat{\boldsymbol{K}}_i, \hat{\boldsymbol{K}}_m, \hat{\boldsymbol{K}}_s \,\middle|\, s_1^{0c}, s_2^{0c}, z_{21}\right)\right\rangle \langle \exp[mj(q-q')z_{21}]\rangle, \end{aligned} \tag{10}$$

where $\langle \exp[mj(q-q')z_{21}]\rangle = \exp\left[-(q-q')^2\sigma_h^2\right]$, for which σ_h^2 is the height variance. This assumption is analysed in appendix B and leads to an overestimation of the modulus.

For the positive path ($m = +$), the average shadowing function $\langle S_c\rangle$ is given by (55) and (57) of [7] for $\varphi_s = \varphi_i$ and $\{\varphi_s \neq \varphi_i, \varphi_s \neq \varphi_i + \pi\}$, respectively. For $\varphi_s = \varphi_i + \pi$, $\langle S_c\rangle$ is similar to $\langle S_c\rangle$ obtained for $\varphi_s = \varphi_i$ where the ranges over the scattering angle θ_s are given by (49) of [7]. Since the surface is assumed to be statistically even, we get for the negative path ($m = -$) $\langle S_c\rangle = S_{2-}\left(\hat{\boldsymbol{K}}_i, \hat{\boldsymbol{K}}_-, \hat{\boldsymbol{K}}_s \,\middle|\, s_1^{0c}, s_2^{0c}\right) = S_{2+}\left(\hat{\boldsymbol{K}}_s, \hat{\boldsymbol{K}}_+, \hat{\boldsymbol{K}}_i \,\middle|\, s_1^{0c}, s_2^{0c}\right)$, which is similar to the transposition of the transmitter with the receiver.

Applying the same way as previously for the derivation of $\langle\cdots\rangle$ in (5), we have

$$\begin{aligned}&\langle S_a \exp[\,\mathrm{j}(q-q'-q_i-q_s)z_{21}]\rangle \\ &\qquad \approx S_{2-}\left(\hat{\boldsymbol{K}}_i, \hat{\boldsymbol{K}}_-, \hat{\boldsymbol{K}}_s \,\middle|\, s_1^{0a}, s_2^{0a}\right) \langle \exp[\,\mathrm{j}(q-q'-q_i-q_s)z_{21}]\rangle \\ &\qquad = S_{2-}\left(\hat{\boldsymbol{K}}_i, \hat{\boldsymbol{K}}'_-, \hat{\boldsymbol{K}}_s \,\middle|\, s_1^{0c}, s_2^{0c}\right) \exp\left[-(q-q'-q_i-q_s)^2\sigma_h^2\right]. \end{aligned} \tag{11}$$

We can note that $S_{2-}\left(\hat{\boldsymbol{K}}_i, \hat{\boldsymbol{K}}'_-, \hat{\boldsymbol{K}}_s \,\middle|\, s_2^{0a}, s_2^{0c}\right) = S_{2-}\left(\hat{\boldsymbol{K}}_i, \hat{\boldsymbol{K}}'_-, \hat{\boldsymbol{K}}_s \,\middle|\, s_1^{0c}, s_2^{0c}\right)$ because there is no restriction over the surface slopes.

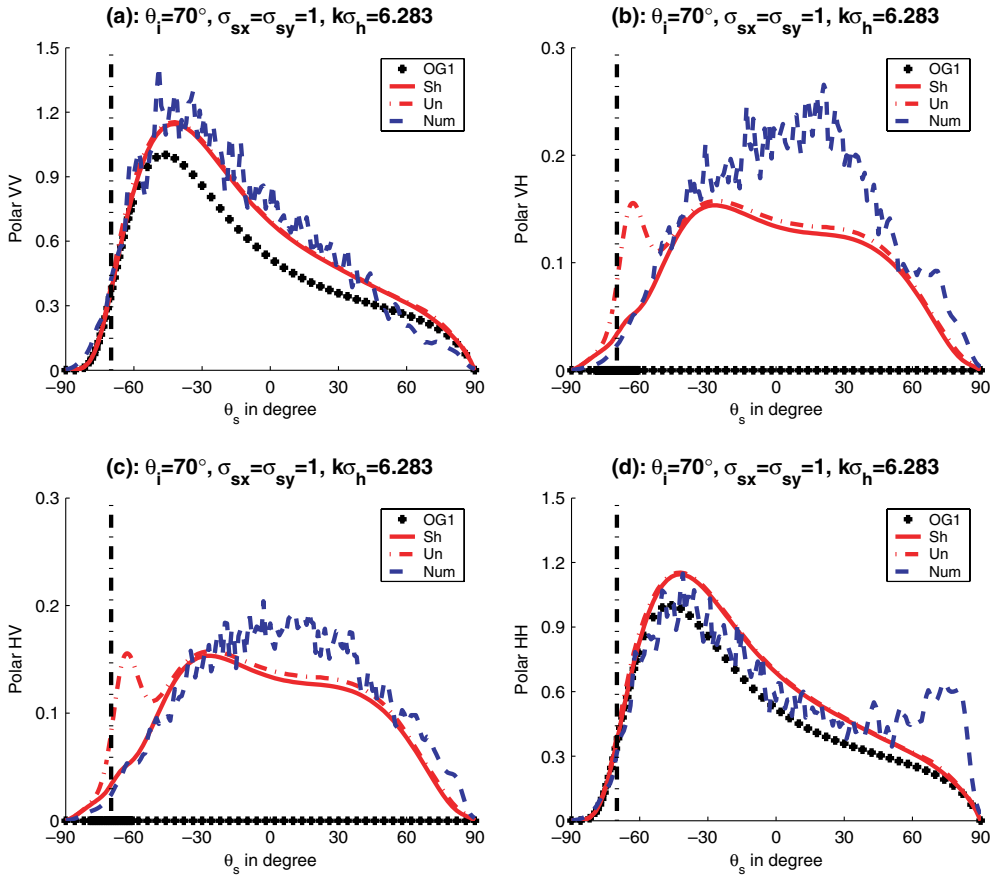

Figure 11. Same variation as figure 8 but $\theta_i = 70^\circ$.

3. Illustrative examples

This section is devoted to the comparison of the second-order geometric optics approximation referred to as OG2 with numerical results obtained from the forward–backward method with a novel spectral acceleration algorithm developed by Torrungrueng and Johnson [1].

3.1. Simulations of OG2 and first-order incoherent scattering coefficient denoted as OG1

In what follows, the simulation parameters are summarized in table 1 where a metallic Gaussian anisotropic surface is considered with a height correlation assumed to be Gaussian.

3.1.1. Comparison for a metallic isotropic surface in the incidence plane where $\varphi_s = \varphi_i = 0^\circ$. In figure 2, the incoherent scattering coefficient σ_{VV} in VV polarization computed from the second-order geometric optics approximation (denoted as OG2) is plotted versus the scattering angle θ_s for an isotropic ($\sigma_{sx} = \sigma_{sy} \Rightarrow L_{cx} = L_{cy}$) metallic surface. At the top, the incidence angle $\theta_i = 0^\circ$, whereas at the bottom $\theta_i = 40^\circ$. On the left, $\sigma_{sx} = 1$ and $k\sigma_h = 2\pi \Rightarrow \sigma_h/\lambda = 1$ (wave number k multiplied by rms height σ_h), whereas on the right, $\sigma_{sx} = 0.5$ and $k\sigma_h = \pi \Rightarrow \sigma_h/\lambda = 0.5$. OG1 gives the contribution of the first

Table 1. Simulation parameters of figures 2–7. The surface is assumed to be Gaussian with an anisotropic height correlation also assumed to be Gaussian ($\sigma_{sx,sy} = \sigma_h\sqrt{2}/L_{cx,cy}$). θ_i is the incidence angle, $\{\sigma_{sx}, \sigma_{sy}\}$ are the rms slopes defined along the $\{\hat{\boldsymbol{x}}, \hat{\boldsymbol{y}}\}$ directions, σ_h/λ is the ratio of the rms height σ_h to the electromagnetic wavelength λ and $\{L_{cx}, L_{cy}\}$ are the correlation lengths along the $\{\hat{\boldsymbol{x}}, \hat{\boldsymbol{y}}\}$ directions. For all figures, azimuthal direction of the emitter is $\varphi_i = 0^\circ$ and a metallic surface is considered.

	θ_i°	φ_s°	σ_{sx}	σ_{sy}	σ_h/λ	l_m/L_{cx}	Polarization
Figure 2(a)	0	0	1	1	1	11.13, 20, 30	VV
Figure 3(a)	0	0	1	1	1	11.13, 20, 30	VH
Figure 2(b)	0	0	0.5	0.5	0.5	11.13, 20, 30	VV
Figure 3(b)	0	0	0.5	0.5	0.5	11.13, 20, 30	VH
Figure 2(c)	40	0	1	1	1	11.13, 20, 30	VV
Figure 3(c)	40	0	1	1	1	11.13, 20, 30	VH
Figure 2(d)	40	0	0.5	0.5	0.5	11.13, 20, 30	VV
Figure 3(d)	40	0	0.5	0.5	0.5	11.13, 20, 30	VH
Figure 4(a)	0	0, 45, 90	1	1	1	11.13	VV
Figure 5(a)	0	0, 45, 90	1	1	1	11.13	VH
Figure 4(b)	0	0, 45, 90	0.5	0.5	0.5	11.13	VV
Figure 5(b)	0	0, 45, 90	0.5	0.5	0.5	11.13	VH
Figure 4(c)	40	0, 45, 90	1	1	1	11.13	VV
Figure 5(c)	40	0, 45, 90	1	1	1	11.13	VH
Figure 4(d)	40	0, 45, 90	0.5	0.5	0.5	11.13	VV
Figure 5(d)	40	0, 45, 90	0.5	0.5	0.5	11.13	VH
Figure 6(a)	0	0	0.5	0.5, 0.7, 0.9	1	11.13	VV
Figure 7(a)	0	0	0.5	0.5, 0.7, 0.9	1	11.13	VH
Figure 6(b)	0	0	0.5	0.5, 0.7, 0.9	0.5	11.13	VV
Figure 7(b)	0	0	0.5	0.5, 0.7, 0.9	0.5	11.13	VH
Figure 6(c)	40	0	0.5	0.5, 0.7, 0.9	1	11.13	VV
Figure 7(c)	40	0	0.5	0.5, 0.7, 0.9	1	11.13	VH
Figure 6(d)	40	0	0.5	0.5, 0.7, 0.9	0.5	11.13	VV
Figure 7(d)	40	0	0.5	0.5, 0.7, 0.9	0.5	11.13	VH

order. In the legend, 'Num' indicates that the mean path length l_m is derived numerically from appendix C, else it is equal to $l_m/L_c = \{11.13, 20, 30\}$ as mentioned in the legend. In figure 3, the same variation is represented in VH polarization. Since for a metallic surface the Fresnel coefficients obey to $|R_{\mathrm{V}}| = |R_{\mathrm{H}}| = 1$, the components in HV and HH polarizations are not displayed ($\sigma_{\mathrm{HH}} = \sigma_{\mathrm{VV}}, \sigma_{\mathrm{VH}} = \sigma_{\mathrm{HV}}$).

As expected, an enhancement is observed in the backscattering direction provided by the contribution of the anticoincidental waves. However, for figures 2(d) and 3(d) any peak is observed in the backscattering direction. The results computed with $l_m = 11.13L_{cx}$ are similar to those obtained when l_m is determined numerically. As l_m increases, the magnitude increases weakly whereas the angular width of the peak varies insignificantly. Therefore in what follows, we will set $l_m = 11.13L_c$.

As depicted in figure 3, since the azimuthal angles $\varphi_s = \varphi_i$, the contribution of OG1 in VH polarization is nil. This shows that the backscattering enhancement effect is related to the multiple scattering and we can observe that the ratio $\sigma_{\mathrm{VH}}/\sigma_{\mathrm{VV}}$ is of the order 0.5.

3.1.2. Comparison for a metallic isotropic surface where the transmitter is out of the incidence plane. In figures 4 and 5, same variation as in figures 2 and 3 is plotted for VV and VH polarizations with $\varphi_s = \{0, 45, 90\}^\circ$ (indicated in the legend), $\varphi_i = 0^\circ$ and $l_m = 11.13L_{cx}$. As φ_s increases, the magnitude decreases for VV polarization whereas it increases for VH

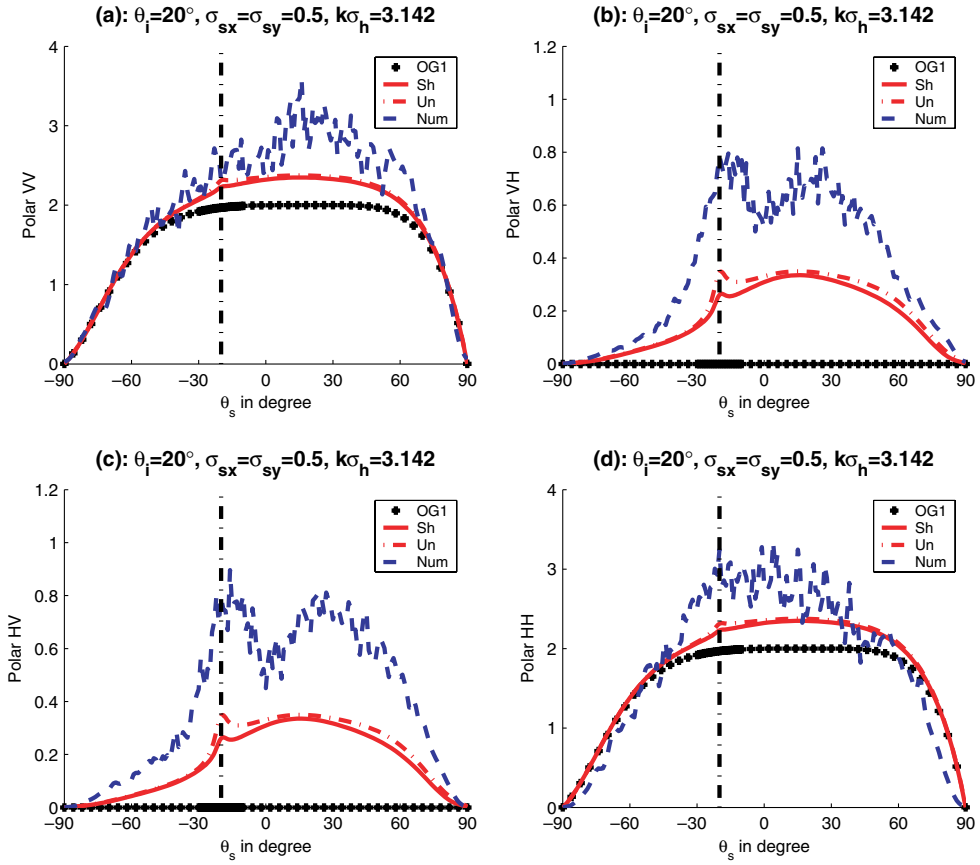

Figure 12. Comparison of the geometric optics approximation denoted as 'OG1' (first order), 'Sh' (first and second orders with shadow) and 'Un' (first and second orders without shadow) with numerical results [1] referred to as 'Num' for {VV (a), VH (b), HV (c), HH (d)} polarizations. The surface is assumed to be metallic and isotropic. $l_m = 11.13L_{cx}, \sigma_{sy} = \sigma_{sx} = 0.5, k\sigma_h = \pi \Rightarrow \sigma_h/\lambda = 0.5$ and incidence angle $\theta_i = 20^\circ$.

polarization because the first-order contribution becomes significant. However, for any polarization and for $\theta_i = 40^\circ$, when φ_s increases the level and the angular width of the backscattering peak decrease noticeably.

3.1.3. Comparison for a metallic anisotropic surface in the incidence plane where $\varphi_s = \varphi_i = 0^\circ$. In figures 6 and 7, same variation as in figures 2 and 3 is represented for VV and VH polarizations with $\sigma_{sy} = \{0.5, 0.7, 0.9\}$ (indicated in the legend), $l_m = 11.13L_{cx}$, $\varphi_s = 0^\circ$ and $\sigma_{sx} = 0.5$. When σ_{sy} increases, the patterns increase for all scattering angles for the VH polarization, whereas for grazing scattering angles, the patterns become smaller for the VV polarization.

3.2. Comparison with numerical results for a Gaussian isotropic surface in the incidence plane where $\varphi_s = \varphi_i = 0^\circ$

The simulation parameters are summarized in table 2. The numerical results are provided by Torrungrueng and Johnson [1], for which the height correlation is considered as Gaussian

Table 2. Simulation parameters of figures 8–19. The surface is assumed to be Gaussian with an isotropic height correlation also assumed to be Gaussian ($\sigma_{sx} = \sigma_h\sqrt{2}/L_{cx}$ with $\sigma_{sx} = \sigma_{sy}$ and $L_{cx} = L_{cy}$). θ_i is the incidence angle, σ_{sx} is the rms slope defined along the $\hat{\boldsymbol{x}}$ direction, σ_h/λ is the ratio of the rms height σ_h to the electromagnetic wavelength λ and $L_{cx} = \lambda\sqrt{2}$ is the correlation length along the $\hat{\boldsymbol{x}}$ direction. For all figures, the four polarizations {VV, VH, HV, HH} are depicted and the emitter and the transmitter are located in the same plane where $\varphi_s = \varphi_i = 0^\circ$.

	θ_i	σ_{sx}	σ_h/λ	Permittivity ε_r
Figure 8	0°	1	1	$i\infty$
Figure 9	20°	1	1	$i\infty$
Figure 10	40°	1	1	$i\infty$
Figure 11	70°	1	1	$i\infty$
Figure 12	20°	0.5	0.5	$i\infty$
Figure 13	20°	$1/\sqrt{2}$	$1/\sqrt{2}$	$i\infty$
Figure 14	70°	0.5	0.5	$i\infty$
Figure 15	70°	$1/\sqrt{2}$	$1/\sqrt{2}$	$i\infty$
Figure 16	20°	1	1	$10 + i10$
Figure 17	60°	1	1	$10 + i10$
Figure 18	20°	1	1	$38 + i40$
Figure 19	60°	1	1	$38 + i40$

and the correlation length $L_{cx} = L_{cy} = \lambda\sqrt{2}$ where λ is the electromagnetic wavelength. The purpose of this subsection is to compare our model with numerical results based on the forward–backward method with a novel spectral acceleration algorithm.

3.2.1. Case of a metallic surface. In figure 8, the geometric optics approximation denoted as 'OG1' (first-order), 'Sh' (first and second orders where the shadowing effect is taken into account) and 'Un' (first and second orders where the shadowing effect is omitted) is compared with numerical results [1] referred to as 'Num' for {VV (a), VH (b), HV (c), HH (d)} polarizations. The mean path length $l_m = 11.13L_{cx}$, the rms slopes $\sigma_{sy} = \sigma_{sx} = 1$, the product $k\sigma_h = 2\pi \Rightarrow \sigma_h/\lambda = 1$ and the incidence angle $\theta_i = 0^\circ$. In figures 9 and 10, the same variation is represented for $\theta_i = \{20, 40\}^\circ$, respectively.

As the incident angle increases, the overall incoherent scattering coefficient level tends to decrease. The deviation between the numerical results and OG2 decreases when the incident angle increases since the contribution of the higher order scattering diminishes and the difference is less for the co-polarizations.

In figure 12, the geometric optics approximation denoted as 'OG1' (first order), 'Sh' (first and second orders where the shadowing effect is taken into account) and 'Un' (first and second orders where the shadowing effect is omitted) is compared with numerical results [1] referred to as 'Num' for {VV (a), VH (b), HV (c), HH (d)} polarizations. $l_m = 11.13L_{cx}$, $\sigma_{sy} = \sigma_{sx} = 0.5$, $k\sigma_h = \pi \Rightarrow \sigma_h/\lambda = 0.5$ and $\theta_i = 20^\circ$. In figure 13, the same variation is represented with $\sigma_{sy} = \sigma_{sx} = 1/\sqrt{2}$, $k_0\sigma_h = \pi\sqrt{2} \Rightarrow \sigma_h/\lambda = 1/\sqrt{2}$. As shown in table 2, for figures 9, 12 and 13, the incidence angle is $\theta_i = 20^\circ$. For these figures, when the rms slope decreases (or $k\sigma_h$ decreases) better agreement between the numerical data and OG2 model is obtained for the co-polarizations and the peak level weakly decreases.

In figures 14 and 15, the same variation is plotted as in figures 12 and 13 with $\theta_i = 70^\circ$, respectively. As shown in table 2, for figures 11, 14 and 15, the incidence angle is $\theta_i = 70^\circ$. Comparing these figures with figures 9, 12 and 13 where $\theta_i = 20^\circ$, we can observe that when θ_i increases better agreement between OG2 and numerical results is obtained for

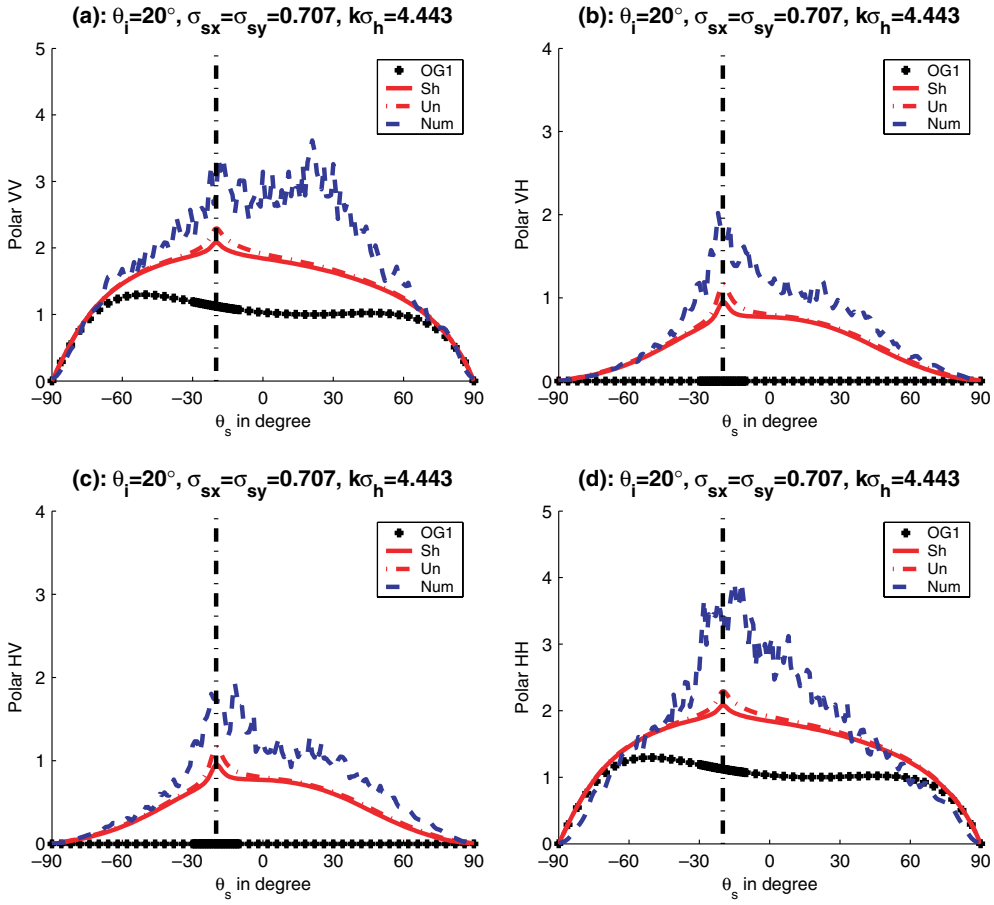

Figure 13. Same variation as figure 12 but $\sigma_{sy} = \sigma_{sx} = \sqrt{2}$, $k_0\sigma_h = \pi\sqrt{2} \Rightarrow \sigma_h/\lambda = 1/\sqrt{2}$.

co-polarizations. Moreover, for figures 11(d), 14(d) and 15(d) in HH polarization, around the specular direction numerical results exhibit more scattered energy than the OG2 model.

From figures 8–15, when the shadowing effect is included the level decreases weakly around the backscattering direction except for $\theta_i = 70°$, where the shadow is needed.

3.2.2. Case of a dielectric surface. In figures 16 and 17, the geometric optics approximation denoted as 'OG1' (first-order), 'Sh' (first and second orders where the shadowing effect is taken into account) and 'Un' (first and second orders where the shadowing effect is omitted) is compared with numerical results [1] referred to as 'Num' for {VV (a), VH (b), HV (c), HH (d)} polarizations. The surface is isotropic and dielectric with $\varepsilon_r = 10 + i10$. $l_m = 11.13L_{cx}$, $\sigma_{sy} = \sigma_{sx} = 1$, $k\sigma_h = 2\pi \Rightarrow \sigma_h/\lambda = 1$ and incidence angle $\theta_i = 20°$. In figures 18 and 19, the same variation as in figures 16 and 17 is displayed with $\varepsilon_r = 38 + i40$. From these figures and figure 9 where $\theta_i = 20°$ and $\varepsilon_r = i\infty$, we can see that the overall bistatic incoherent scattering coefficient level increases as the surface material becomes denser ($|\varepsilon_r|$ increases) because the modulus of the Fresnel coefficients increases. In addition, when $|\varepsilon_r|$ decreases the agreement between the OG2 model and numerical results becomes better since the contribution of the higher order reflection is less important. As previously mentioned, the shadowing effect can be omitted.

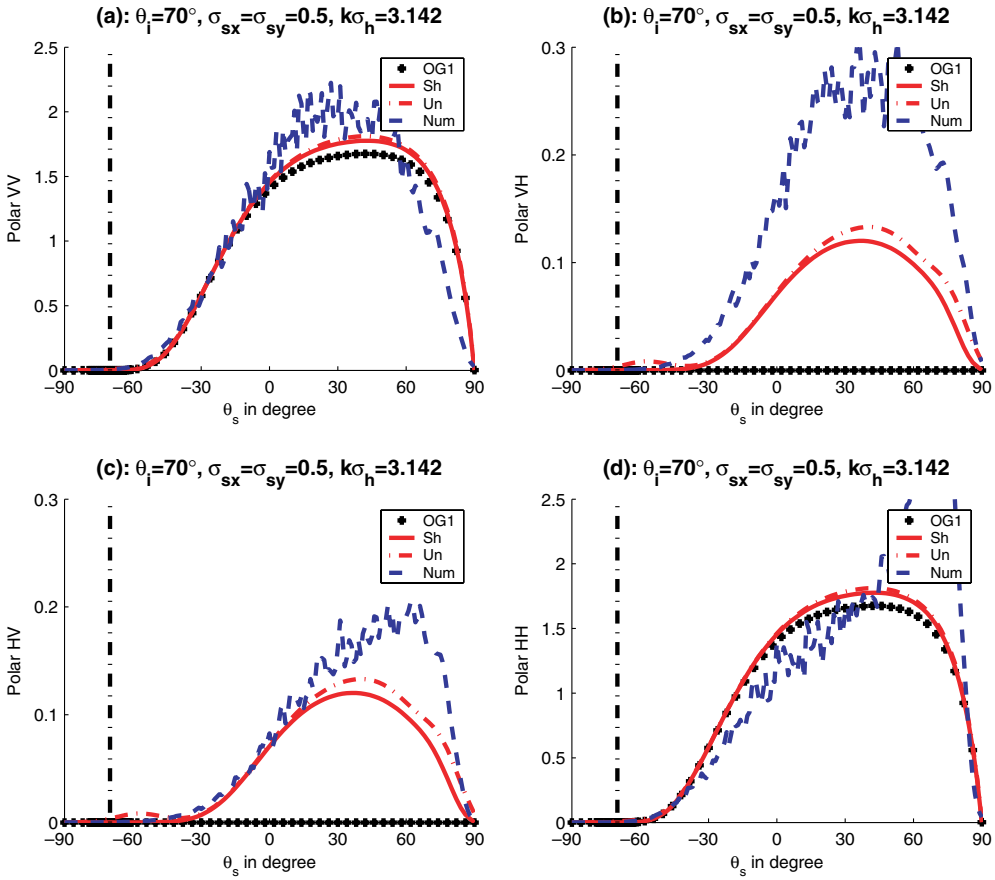

Figure 14. Same variation as figure 12 but $\theta_i = 70^\circ$.

4. Conclusion

We present an analytical theory for polarimetric scattering by 2D dimensional anisotropic Gaussian surface. The model is based on the first- and second-order optics approximations where the shadowing effect is taken into account within the first- and second-order illumination functions. The computation of the incoherent scattering coefficient then required only three-fold integrations allowing us to have a small computer time. In addition, this model predicts the backscattering enhancement phenomenon for a slope rms range from 0.5 to 1 and a height rms range from 0.5λ to 1λ (where λ is the electromagnetic wavelength).

The simulations show that the cross-polarizations exhibit energy although there is no first-order contribution. The backscattering peak level is related to the difference of the azimuthal directions $\varphi_s - \varphi_i$ between the receiver and the transmitter. As incident angle increases, smaller backscattering enhancement effects are observed, even when the very rough and large-slope surfaces are considered. The incoherent scattering coefficient tends to increase as surfaces become denser since it is expressed from the Fresnel coefficients. For moderate incident angles, we can observe that the shadowing effect can be neglected. However, if the shadow is taken into account, the level decreases weakly around the backscattering direction and for grazing incident angle the shadow must be included.

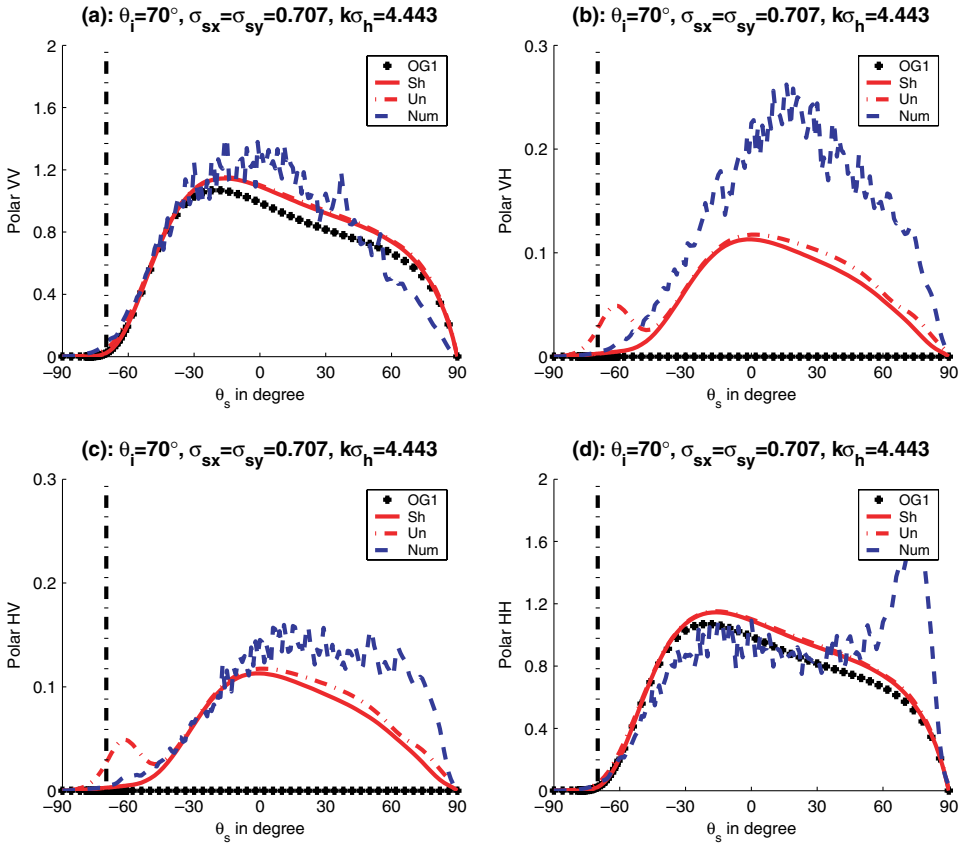

Figure 15. Same variation as figure 13 but $\theta_i = 70^\circ$.

From the numerical results, a general conclusion of the applicability of the method can be the following. For rms slope equal to 1, the model can be applied for incident angles $\theta_{i,l}$ greater than 40°, for which the higher order contributions vanish. This means that if the rms slope diminishes, then the lower limit $\theta_{i,l}$ should decrease. From the simulations, this point is not verified (for instance, see figure 12) since $k\sigma_h$ is not large enough to use the geometric optics approximation. Thus, the first restriction of the model seems to be that $k\sigma_h$ must be greater that 2π. According to the surface slope, greater the rms slope, larger the incident angle, in order to eliminate the higher order contributions. For a dielectric surface, $\theta_{i,l}$ decreases when $|\varepsilon_r|$ decreases because a part of energy is transmitted in the lower medium leading to the higher order contributions vanishing more quickly.

Acknowledgments

The authors would like to thank Dr Torrungrueng and Professor Johnson for providing us their numerical results.

Appendix A. Calculation of the integration over the azimuthal direction φ

The computation of the coincidental σ_{2c} and anticoincidental σ_{2a} contributions given by (5) and (6) require four-fold integrations over $\{\theta, \theta', \varphi, \varphi'\}$. By using (8) we can calculate the

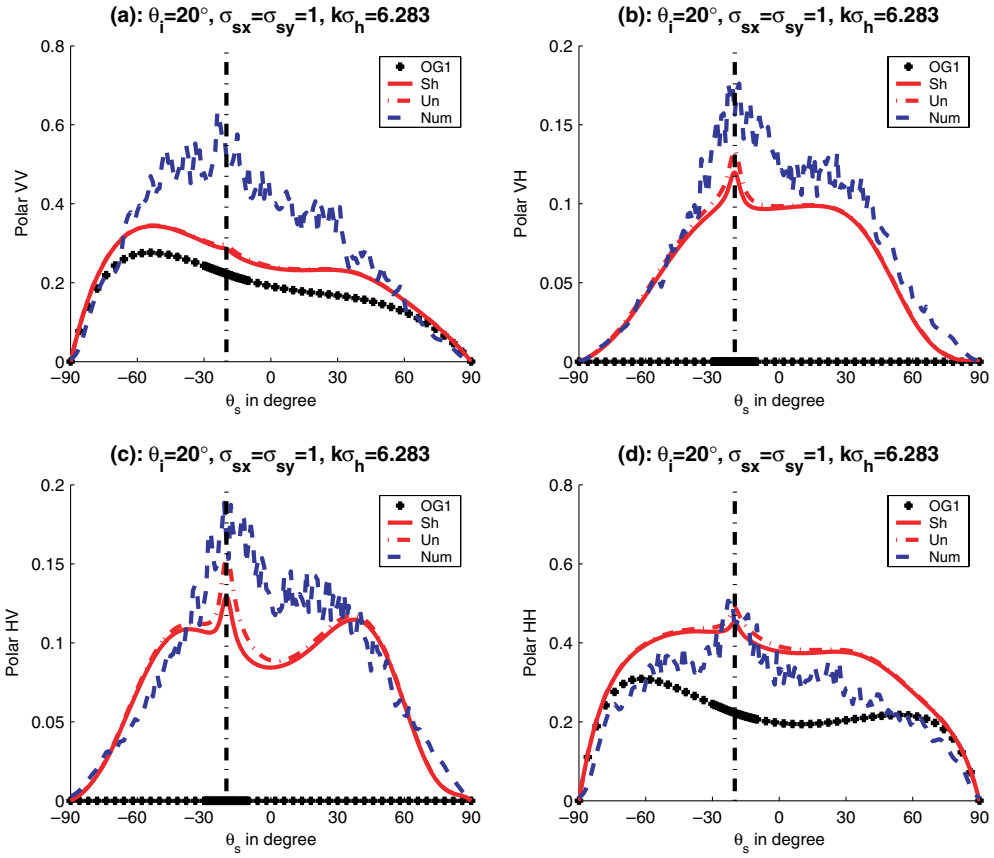

Figure 16. Comparison of the geometric optics approximation denoted as 'OG1' (first order) and 'OG2' (first and second orders) with numerical results [1] referred to as 'Num' for {VV (a), VH (b), HV (c), HH (d)} polarizations. The surface is assumed to be dielectric with $\varepsilon_r = 10 + i10$ and isotropic. $l_m = 11.13L_{cx}, \sigma_{sy} = \sigma_{sx} = 1, k\sigma_h = 2\pi \Rightarrow \sigma_h/\lambda = 1$ and incidence angle $\theta_i = 20^\circ$.

integration over φ' where $\boldsymbol{u} = \boldsymbol{k} - \boldsymbol{k}'$, for the coincidental waves and $\boldsymbol{u} = \boldsymbol{k} + \boldsymbol{k}' - \boldsymbol{k}_i - \boldsymbol{k}_s$, for the anticoincidental waves. Thus, substituting (8) into either (5) or (6), the integral over φ' is written as

$$\Psi = \frac{(k_0 l_m)^2}{\pi} \int_0^{2\pi} \exp\left\{-\frac{l_m^2}{2}[(k_x+\alpha)^2 + (k_y+\beta)^2]\right\} \mathrm{d}\varphi, \tag{A1}$$

where

$$\alpha = -k'_x, \qquad \beta = -k'_y \quad \text{for the coincidental waves,} \tag{A2}$$

$$\alpha = k'_x - k_{ix} - k_{sx}, \qquad \beta = k'_y - k_{iy} - k_{sy} \quad \text{for the anticoincidental waves.} \tag{A3}$$

Using the expressions of the components of $\{k_{ix,sx,iy,sy}\}$ and $\{k'_{x,y}\}$, (A1) takes the form

$$\Psi = \frac{(k_0 l_m)^2}{\pi} \exp\left\{-\frac{l_m^2}{2}[(\sin\theta')^2 + \alpha^2 + \beta^2]\right\} \times \int_0^{2\pi} \exp\left[-l_m^2(\alpha^2+\beta^2)^{1/2} \sin\theta' \cos(\varphi - \chi)\right] \mathrm{d}\varphi, \tag{A4}$$

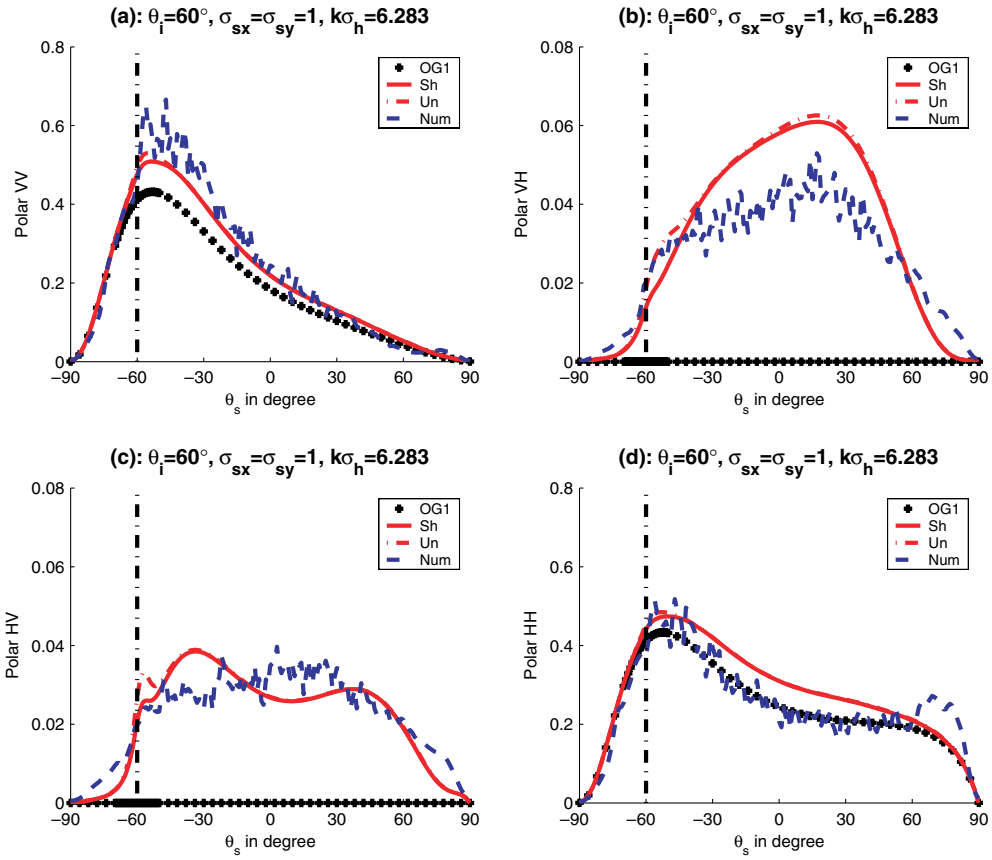

Figure 17. Same variation as figure 16 but $\theta_i = 60^\circ$.

where $\tan\chi = \beta/\alpha$. Using the following relation:

$$J_0(x) = \frac{1}{2\pi}\int_0^{2\pi} \exp[\,\mathrm{j}x\cos(\varphi-\chi)]\,\mathrm{d}\varphi, \tag{A5}$$

where J_0 is the Bessel function of the first kind and zero order, leads to

$$\Psi = 2(k_0 l_m)^2 \exp\left\{-\frac{l_m^2}{2}[(\sin\theta')^2+\alpha^2+\beta^2]\right\} I_0\big(l_m^2[\alpha^2+\beta^2]^{1/2}\sin\theta'\big). \tag{A6}$$

$I_0(x) = J_0(\mathrm{j}x)$ is the modified Bessel function of the first kind and zero order. The computation of $\{\sigma_{2c}, \sigma_{2a}\}$ now requires three-fold numerical integrations.

Appendix B. Study of the assumption used for the calculation of the ensemble average

To study assumption (10), the following expected value is computed:

$$\begin{aligned}\Theta_m &= \left\langle S_c\big(\hat{\boldsymbol{K}}_i, \hat{\boldsymbol{K}}_m, \hat{\boldsymbol{K}}_s \,\big|\, \boldsymbol{s}_1^{0c}, \boldsymbol{s}_2^{0c}, z_{21}\big)\exp(\,\mathrm{j}\alpha z_{2l})\right\rangle \\ &= \int_{-\infty}^{\infty}\mathrm{d}z_1 \int_{z_{2l}}^{z_{2u}} \exp[\,\mathrm{j}\alpha(z_2-z_1)] S_{2m}\big(\hat{\boldsymbol{K}}_i, \hat{\boldsymbol{K}}_m, \hat{\boldsymbol{K}}_s \,\big|\, \boldsymbol{s}_1^{0c}, \boldsymbol{s}_2^{0c}, z_{21}\big) p_h(z_1, z_2)\,\mathrm{d}z_2, \end{aligned} \tag{B1}$$

where $p_h(z_1, z_2)$ is the height joint distribution and $S_{2m}\big(\hat{\boldsymbol{K}}_i, \hat{\boldsymbol{K}}_m, \hat{\boldsymbol{K}}_s \,\big|\, \boldsymbol{s}_1^{0c}, \boldsymbol{s}_2^{0c}, z_{21}\big)$ is the second-order statistical shadowing function. In addition, for $m = +$, $\{z_{2l} = z_1, z_{2u} = \infty\}$ and

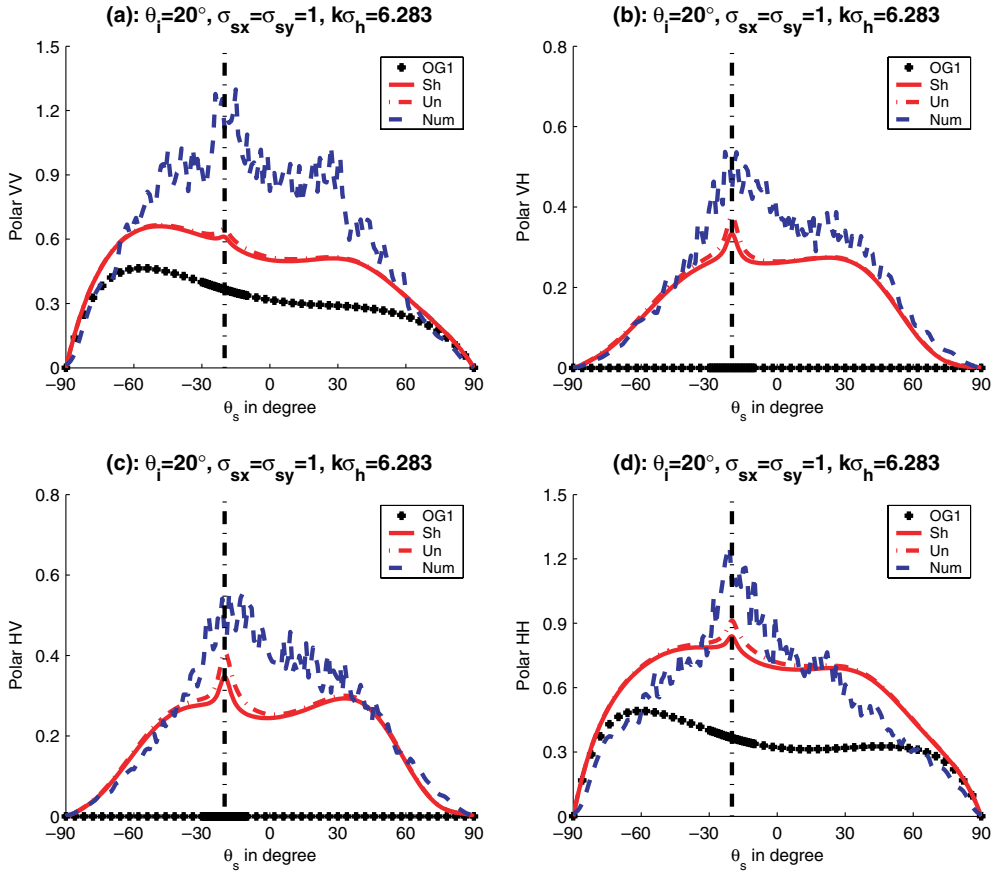

Figure 18. Same variation as figure 16 but $\varepsilon_r = 38 + i40$.

for $m = -$, $\{z_{2l} = -\infty, z_{2u} = z_1\}$. Thus, for a Gaussian process, we have for $m = +$ with the variable transformations $h_i = z_i/(\sigma_h\sqrt{2})$ (σ_h is the rms height)

$$\Theta_+ = \frac{1}{\pi}\int_{-\infty}^{\infty} \mathrm{d}h_1 \int_{h_1}^{\infty} \exp[\,\mathrm{j}\alpha\sqrt{2}\sigma_h(h_2 - h_1)]\exp\left(-h_1^2 - h_2^2\right) \times S_{2+}\left(\hat{\boldsymbol{K}}_i, \hat{\boldsymbol{K}}_+, \hat{\boldsymbol{K}}_s \,\middle|\, s_1^{0c}, s_2^{0c}, h_{21}\right)\mathrm{d}h_2, \tag{B2}$$

with

$$\text{for} \quad \phi_s = \phi_i, \qquad S_{2+}\left(\hat{\boldsymbol{K}}_i, \hat{\boldsymbol{K}}_+, \hat{\boldsymbol{K}}_s \,\middle|\, s_1^{0c}, s_2^{0c}, h_{21}\right) \tag{B3}$$

$$= \left[1 - \frac{\mathrm{erfc}(h_1)}{2}\right]^{\Lambda(\hat{\boldsymbol{K}}_i)} \left(1 - \left\{\frac{[1 - \mathrm{erfc}(h_1)/2]}{[1 - \mathrm{erfc}(h_2)/2]}\right\}^{\Lambda(\hat{\boldsymbol{K}}_+)}\right) \left[1 - \frac{\mathrm{erfc}(h_2)}{2}\right]^{\Lambda(\hat{\boldsymbol{K}}_s)}$$

$$\text{where} \quad \theta_s \in [0; \pi/2], \tag{B4}$$

$$\left[1 - \frac{\mathrm{erfc}(h_1)}{2}\right]^{\Lambda(\hat{\boldsymbol{K}}_i)} \left(1 - \left\{\frac{[1 - \mathrm{erfc}(h_1)/2]}{[1 - \mathrm{erfc}(h_2)/2]}\right\}^{\Lambda(\hat{\boldsymbol{K}}_+)}\right) \qquad \text{where} \quad \theta_s \in [-\theta_i; 0[, \tag{B5}$$

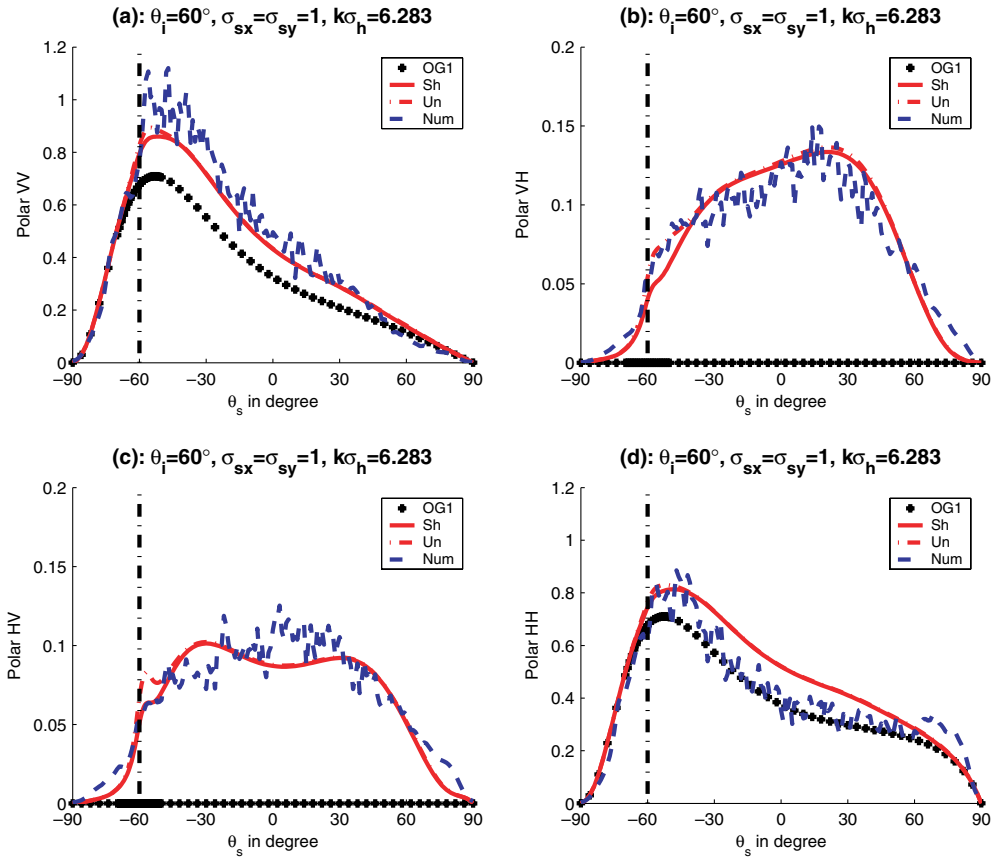

Figure 19. Same variation as figure 17 but $\varepsilon_r = 38 + i40$.

$$\left[1 - \frac{\operatorname{erfc}(h_1)}{2}\right]^{\Lambda(\hat{\boldsymbol{K}}_i)} \left(1 - \left\{\frac{[1 - \operatorname{erfc}(h_1)/2]}{[1 - \operatorname{erfc}(h_2)/2]}\right\}^{\Lambda(\hat{\boldsymbol{K}}_+)}\right) \qquad \text{where} \quad \theta_s \in [-\pi/2; -\theta_i[. \tag{B6}$$

Λ is expressed from (4). Now, assuming in (B2) that the shadow is statistically independent of $\exp(\mathrm{j}\alpha z_{21})$, we get

$$\begin{aligned}\Theta_+ &= \left\langle S_{2+}\left(\hat{\boldsymbol{K}}_i, \hat{\boldsymbol{K}}_+, \hat{\boldsymbol{K}}_s \,\middle|\, \boldsymbol{s}_1^{0c}, \boldsymbol{s}_2^{0c}, z_{21}\right)\right\rangle \langle \exp(\mathrm{j}\alpha z_{21})\rangle \\ &= S_{2+}\left(\hat{\boldsymbol{K}}_i, \hat{\boldsymbol{K}}_+, \hat{\boldsymbol{K}}_s \,\middle|\, \boldsymbol{s}_1^{0c}, \boldsymbol{s}_2^{0c}\right) \exp\left(-\alpha^2\sigma_h^2\right),\end{aligned} \tag{B7}$$

where $S_{2+}\left(\hat{\boldsymbol{K}}_i, \hat{\boldsymbol{K}}_+, \hat{\boldsymbol{K}}_s \,\middle|\, \boldsymbol{s}_1^{0c}, \boldsymbol{s}_2^{0c}\right)$ is given by (55) of [7] for $\varphi_s = \varphi_i$. Therefore, the expected value is given either by (B2), computed numerically, or (B7) computed analytically. It depends on $\{\Lambda(\hat{\boldsymbol{K}}_i), \Lambda(\hat{\boldsymbol{K}}_+), \Lambda(\hat{\boldsymbol{K}}_s)\}$ and $\alpha_h = \alpha\sigma_h$. To reduce the number of freedom degrees for the simulations, we set $\{\Lambda(\hat{\boldsymbol{K}}_{i,s})\} \approx \{0\}$, which means that the transmitter and the receiver illuminate the whole surface. These approximations can be used if $\nu_{i,s} = |\cot\theta_{i,s}| \big/ \left\{2\left[\sigma_{sx}^2(\cos\varphi_i)^2 + \sigma_{sy}^2(\sin\varphi_s)^2\right]\right\}^{1/2}$ is larger than 1.5 ($\Lambda = 0.003$). For instance, for rms slopes $\left[\sigma_{sx}^2(\cos\varphi_i)^2 + \sigma_{sy}^2(\sin\varphi_s)^2\right]^{1/2} = \{0.5, 1\}$, we must have $\{|\theta_{i,s}|\} \leqslant \{43, 25\}^\circ$, respectively.

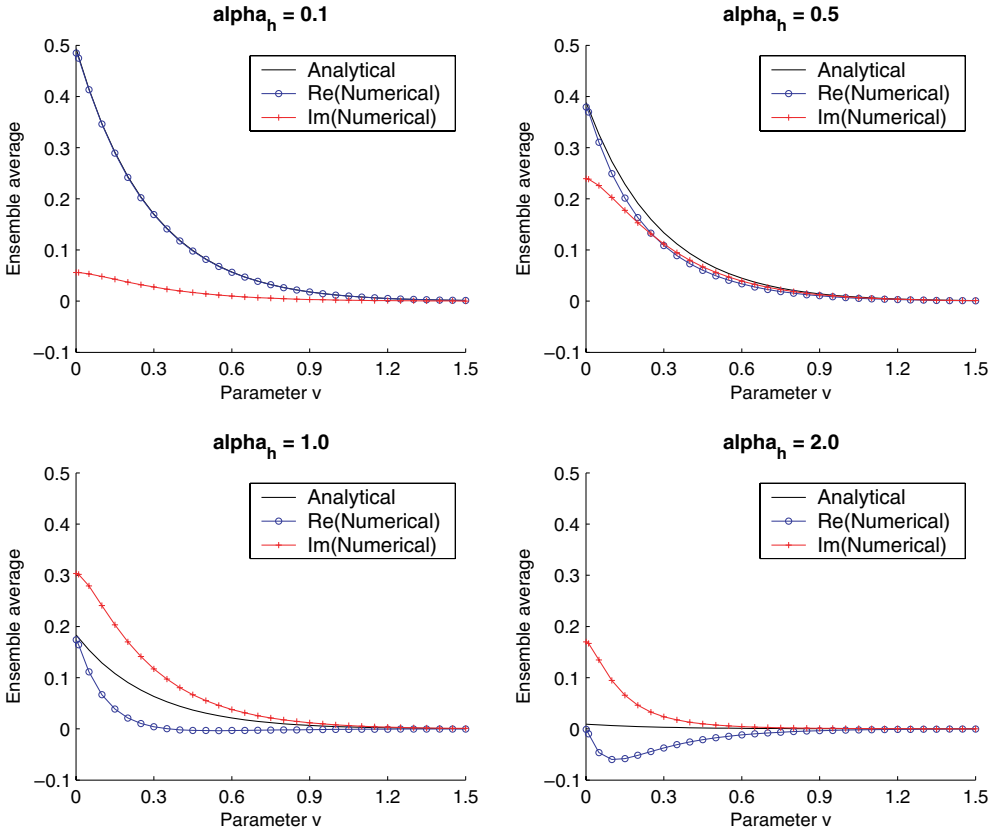

Figure B1. Numerical (circle and cross curves depict its real and imaginary parts, respectively) and analytical (full curve) ensemble averages versus the parameter ν.

In figure B1, the real and imaginary parts of the ensemble average (B2) are compared with analytical equation (B7), which is real, versus the parameter ν with $\alpha_h = \{0.1, 0.5, 1, 2\}$. One can see that for ν greater than 1.5 (corresponding to θ close to 0°, or rms slope small), Θ_+ tends towards zero, since the probability that the ray emanating from the first reflection intercepts the surface is insignificant. For small values of α_h, there is a good agreement between the real part of the numerical results and the analytical ones, while when α_h increases, the deviation between the two quantities increases, and the imaginary part is appreciable. In conclusion, using (B7) leads to an overestimation of the real part of Θ_+ and the imaginary part is equal to zero. Nevertheless, for the simulations (B7) is applied because using (B1) involves two additional numerical integrations which strongly increase the computer time.

Appendix C. Calculation of the mean path length

In this appendix, a method is presented to calculate z_m as functions of the angles $\{\theta, \varphi\}$ and of the slope rms $\{\sigma_{sx}, \sigma_{sy}\}$ defined according to the $\{\hat{\boldsymbol{x}}, \hat{\boldsymbol{y}}\}$ directions. From figure 1, we can write

$$z_m = \langle z_2 - z_1 \rangle = \int_{-\infty}^{\infty} \mathrm{d}z_1 \int_{z_{2l}}^{z_{2u}} \frac{S_{2m}(\hat{\boldsymbol{K}}_i, \hat{\boldsymbol{K}}_m, \hat{\boldsymbol{K}}_s, z_2, z_1)(z_2 - z_1) p_h(z_1, z_2)}{\langle S_{2m}(\hat{\boldsymbol{K}}_i, \hat{\boldsymbol{K}}_m, \hat{\boldsymbol{K}}_s, z_2, z_1) \rangle} \mathrm{d}z_2, \qquad \text{(C1)}$$

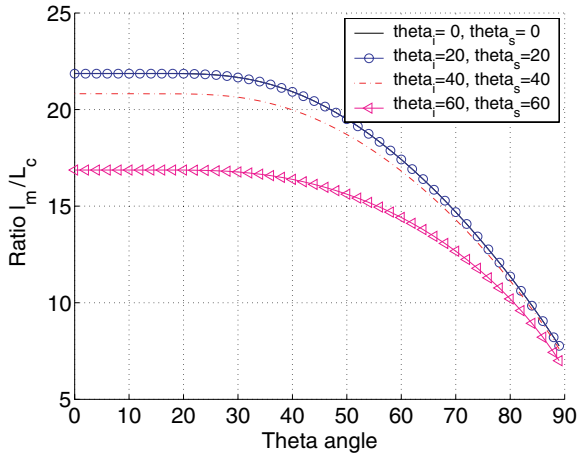

Figure C1. Ratio l_m/L_c defined as the mean path length over the correlation length versus the angle θ. The rms slope $\sigma_{sx} = 1$ and $\theta_s = \theta_i = \{0, 20, 40, 60\}^\circ$ with $\varphi_i = \varphi_s = \varphi = 0$.

where $p_h(z_1, z_2)$ is the height joint distribution and $S_{2m}(\hat{\boldsymbol{K}}_i, \hat{\boldsymbol{K}}_m, \hat{\boldsymbol{K}}_s, z_2, z_1)$ is the second-order statistical shadowing function. In addition, for $m = +$, $\{z_{2l} = z_1, z_{2u} = \infty\}$ and for $m = -$, $\{z_{2l} = -\infty, z_{2u} = z_1\}$. Neglecting the shadow provided by both the transmitter and the receiver ($\theta_i = \theta_s = 0^\circ \Rightarrow \Lambda(\hat{\boldsymbol{K}}_i) = \Lambda(\hat{\boldsymbol{K}}_s) = 0$), and considering an uncorrelated Gaussian process, we have from [7] for the ray positive path

$$\frac{z_+}{\sigma_h\sqrt{2}} = \frac{2[1 + \Lambda(\hat{\boldsymbol{K}}_+)]}{\Lambda(\hat{\boldsymbol{K}}_+)} \int_{-\infty}^{\infty} \mathrm{d}h_1 \int_{h_1}^{\infty} \left\{ 1 - \left[\frac{1 - \mathrm{erfc}(h_1)/2}{1 - \mathrm{erfc}(h_2)/2} \right]^{\Lambda(\hat{\boldsymbol{K}}_+)} \right\} (h_2 - h_1) \times \exp\left(-h_1^2 - h_2^2\right) \mathrm{d}h_2, \tag{C2}$$

where Λ is given by (4). Therefore, $z_+/(\sigma_h\sqrt{2})$ depends on $\{\theta, \varphi, \sigma_{sx}, \sigma_{sy}\}$ within ν expressed from (4). In figure C1, the ratio l_+/L_c computed from (C2) and (9) is plotted versus the angle θ. The full curve is obtained when $\theta_i = \theta_s = 0^\circ$ corresponding to (C2), whereas for the other curves, we have $\theta_s = \theta_i = \{20, 40, 60\}^\circ$ where $S_{2+}(\hat{\boldsymbol{K}}_i, \hat{\boldsymbol{K}}_+, \hat{\boldsymbol{K}}_s, z_2, z_1)$ is performed from (55) of [7]. In addition, the azimuthal angles $\varphi_i = \varphi_s = \varphi = 0$ and $\sigma_{sx} = 1$ which means that $(\sigma_{sx}\cos\varphi)^2 + (\sigma_{sy}\sin\varphi)^2 = \sigma_{sx}^2$. We observe that $\{l_m/L_c\}$ decreases when the $\{\theta, \theta_{i,s}\}$ angles increase since the ratio of the illuminated surface diminishes. There is no discrepancy between the results computed for $\theta_{i,s} = \{0, 20\}^\circ$, because the shadowing effect can be omitted. Indeed, for this case, $\nu_{i,s} = \{4051, 1.9\}$ and $\Lambda(\nu_{i,s}) = \{0, 0.0003\}$, which is much smaller one. Nevertheless, for $\theta_{i,s} = 40^\circ$, we observe a weakly difference, since $\Lambda(\nu_{i,s}) = 0.05$. For the simulations of the incoherent scattering coefficient, (C2) is used.

References

[1] Torrungrueng D and Johnson J T 2001 Numerical studies of backscattering enhancement of electromagnetic waves from two-dimensional random rough surfaces with the forward–backward/novel spectral acceleration method *JOSA* A **18** 2518–26

[2] Ishimaru A, Le C, Kuga Y, Sengers L A and Chan T K 1996 Polarimetric scattering theory for high slope rough surfaces *Prog. Electromagn. Res.* **14** 1–36

[3] Bahar E and El-Shenawee M 2001 Double-scatter cross sections for two-dimensional random rough surfaces that exhibit backscatter enhancement *JOSA* A **18** 108–16

[4] Ishimaru A and Chen J S 1990 Scattering from very rough surfaces based on the modified second-order Kirchhoff approximation with angular and propagation shadowing *J. Acoust. Soc. Am.* **88** 1877–83
[5] Ishimaru A and Chen J S 1991 Scattering from very rough metallic and dielectric surfaces: a theory based on the modified Kirchhoff approximation *Waves Random Media* **1** 21–34
[6] Bahar E and El-Shenawee M 1994 Vertically and horizontally polarized diffuse double-scatter cross sections of one-dimensional random rough surfaces that exhibit enhanced-backscatter-full-wave solutions *JOSA* A **11** 2271–85
[7] Bourlier C and Berginc G 2003 Multiple scattering in the high-frequency limit with second-order shadowing function from 2D anisotropic rough dielectric surfaces: I. Theoretical study *Waves Random Media* **14** 229–52
[8] Bourlier C, Berginc G and Saillard J 2002 One- and two- dimensional shadowing functions for any height and slope stationary uncorrelated surface in the monostatic and bistatic configurations *IEEE Trans. Antennas Propag.* **50** 312–24